Cell Reports

Article

Disrupted glucocorticoid rhythms selectively induce severe skeletal muscle insulin resistance and uncouple obesity from hepatic steatosis

Graphical abstract

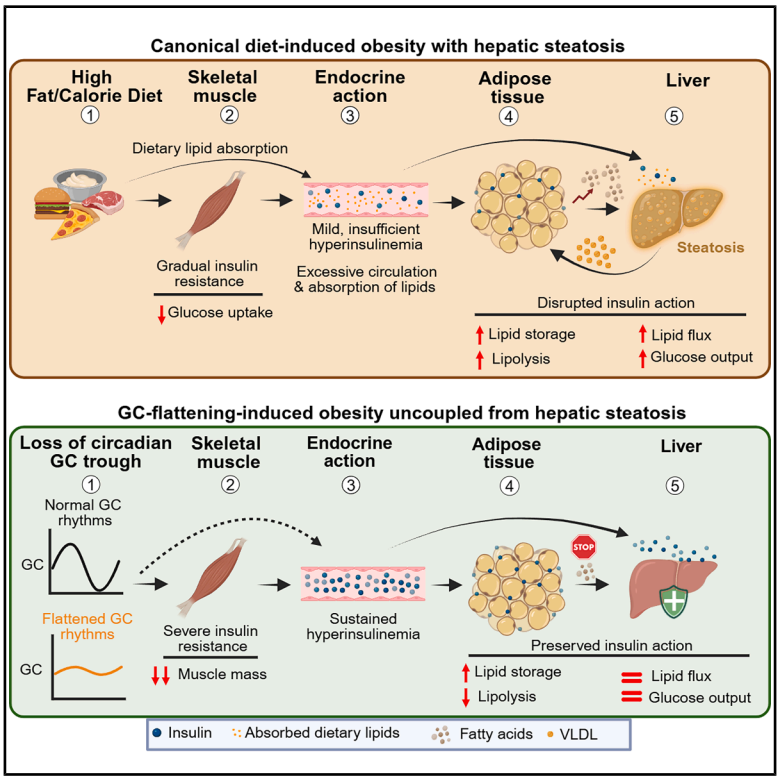

Highlights

- GC-rhythm flattening and high-fat diet act additively to increase total adiposity
- Insulin resistance concentrates in muscle while preserving adipose-liver function
- Insulin-responsive adipose sequesters lipids and shields liver from fatty acids
- Redistributed insulin action uncouples obesity from hepatic steatosis

Authors

Agnieszka Agas, Sanjeev Sharma, Anthony Narciso, ..., Marcus D. Goncalves, Timothy E. McGraw, Mary N. Teruel

Correspondence

mnt4002@med.cornell.edu

In brief

Agas et al. show that flattening daily glucocorticoid rhythms in mice concentrates insulin resistance in skeletal muscle while preserving key adipose-liver functions. Insulin-responsive fat sequesters lipids and shields the liver, uncoupling profound obesity from hepatic steatosis and recasting hyperinsulinemia as protective rather than pathological.

Agas et al., 2026, Cell Reports *45*, 117926
September 22, 2026
https://doi.org/10.1016/j.celrep.2026.117926

CellPress

Cell Reports

CellPress
OPEN ACCESS

Article

Disrupted glucocorticoid rhythms selectively induce severe skeletal muscle insulin resistance and uncouple obesity from hepatic steatosis

Agnieszka Agas,[1,9] Sanjeev Sharma,[1,9] Anthony Narciso,[1] Lucas Paulo Jacinto Saavedra,[1] Jijo Wilson,[1] Jack Lungstrum,[1] Lucie Yammine,[1] Anna S. Arzeno,[1] Louise Lantier,[3] Erin Kilkenny,[1] Ahsan Uddin,[1,8] Carolina E. Echeverria,[4] Katherine R. Ferrick,[1] Isaac Nathoo,[4,6,7] Jonathan Gao,[4] Edmund D. Kapelczak,[5] Rashel Jacobo,[5] Roma Patel,[1] Tara TeSlaa,[5] Marcus D. Goncalves,[4] Timothy E. McGraw,[1] and Mary N. Teruel[1,2,10,*]

[1]Department of Biochemistry and Biophysics, Weill Cornell Medicine, New York, NY 10065, USA
[2]Gale and Ira Drukier Institute for Children's Health, Weill Cornell Medicine, New York, NY 10021, USA
[3]Vanderbilt Mouse Metabolic Phenotyping Center, Vanderbilt University School of Medicine, Nashville, TN 37232, USA
[4]Department of Medicine, New York University Grossman School of Medicine, New York, NY 10016, USA
[5]Department of Molecular and Medical Pharmacology, University of California, Los Angeles, CA 90095, USA
[6]Weill Cornell Graduate School of Medical Sciences, Weill Cornell Medicine, New York, NY 10065, USA
[7]Weill Cornell/Rockefeller/Sloan Kettering Tri-Institutional MD-PhD Program, New York, NY 10065, USA
[8]Department of Pediatrics, NewYork-Presbyterian Hospital/Weill Cornell Medicine, New York, NY 10021, USA
[9]These authors contributed equally
[10]Lead contact
*Correspondence: mnt4002@med.cornell.edu
https://doi.org/10.1016/j.celrep.2026.117926

SUMMARY

Disruption of circadian glucocorticoid (GC) rhythms is associated with chronic stress and obesity, yet its metabolic signature remains poorly defined. Using a physiological mouse model, we show that the liver is largely protected from pathological steatosis despite profound obesity and hyperinsulinemia. We identify a unique redistribution of insulin resistance: rhythm disruption does not globally impair insulin action as occurs in diet-induced obesity. Instead, skeletal muscle develops severe insulin resistance while adipose and hepatic tissues remain functionally insulin responsive. This preserved sensitivity allows the adipose tissue to act as a metabolic reservoir, utilizing sustained hyperinsulinemia to sequester lipids and shield the liver from toxic fatty-acid flux. These findings reveal that GC-rhythm disruption uncouples obesity from hepatic steatosis by redistributing insulin action from skeletal muscle to adipose tissue and liver. Thus, GC-rhythm disruption and high-fat diet are independent and additive drivers of adiposity with divergent hepatic effects.

INTRODUCTION

Obesity is a complex metabolic state that can arise from diverse physiological triggers.[1] While excessive consumption of high-fat diets (HFDs) is often considered a primary driver of the obesity epidemic, substantial evidence points to stress and disrupted sleep as significant, yet understudied, contributing factors.[2,3] Glucocorticoids (GCs) are essential hormones that control whole-body metabolism,[4] and both chronic stress and disrupted sleep have been associated with changes in their daily secretory pattern.[5,6]

In healthy humans, GCs are secreted in circadian oscillations that peak around 7 a.m. and are lowest at night.[7] Chronic stressors, such as shift work[8] and poor sleep quality,[5,9] flatten this rhythm—chiefly by raising evening and nocturnal cortisol and suppressing-, the morning peak. We refer to this blunting of the daily GC rhythm as GC rhythm flattening (GC-flattening, Figure 1A). Previous work has demonstrated that GC-flattening is sufficient to drive rapid expansion of adipose tissue mass in mice,[10,11] independent of increased caloric intake or decreased energy expenditure.[11] Notably, the metabolic effects of GC-flattening depend on loss of the trough rather than on changes in the peak[6,12], as demonstrated by the fact that substantially raising the GC peak while preserving the trough does not reproduce the gains in fat mass or body weight observed with GC-flattening.[11] Although the causal contribution of loss of the daily GC trough cannot be directly tested in humans, the cortisol rhythm disruption seen with shift work[8] and chronic stress has been shown to be associated with obesity and abdominal adiposity,[13,14] implicating GC rhythm disruption in human metabolic disease.

Importantly, GC-flattening rarely occurs in isolation. In contemporary society, stress-mediated hormonal disruption can occur alongside widespread consumption of high fat diets.[15–18] While both flattened GC rhythms and HFD consumption are established drivers of adiposity, it remains unclear whether they converge on a singular metabolic pathway or act via independent mechanisms. Identifying the distinct processes by

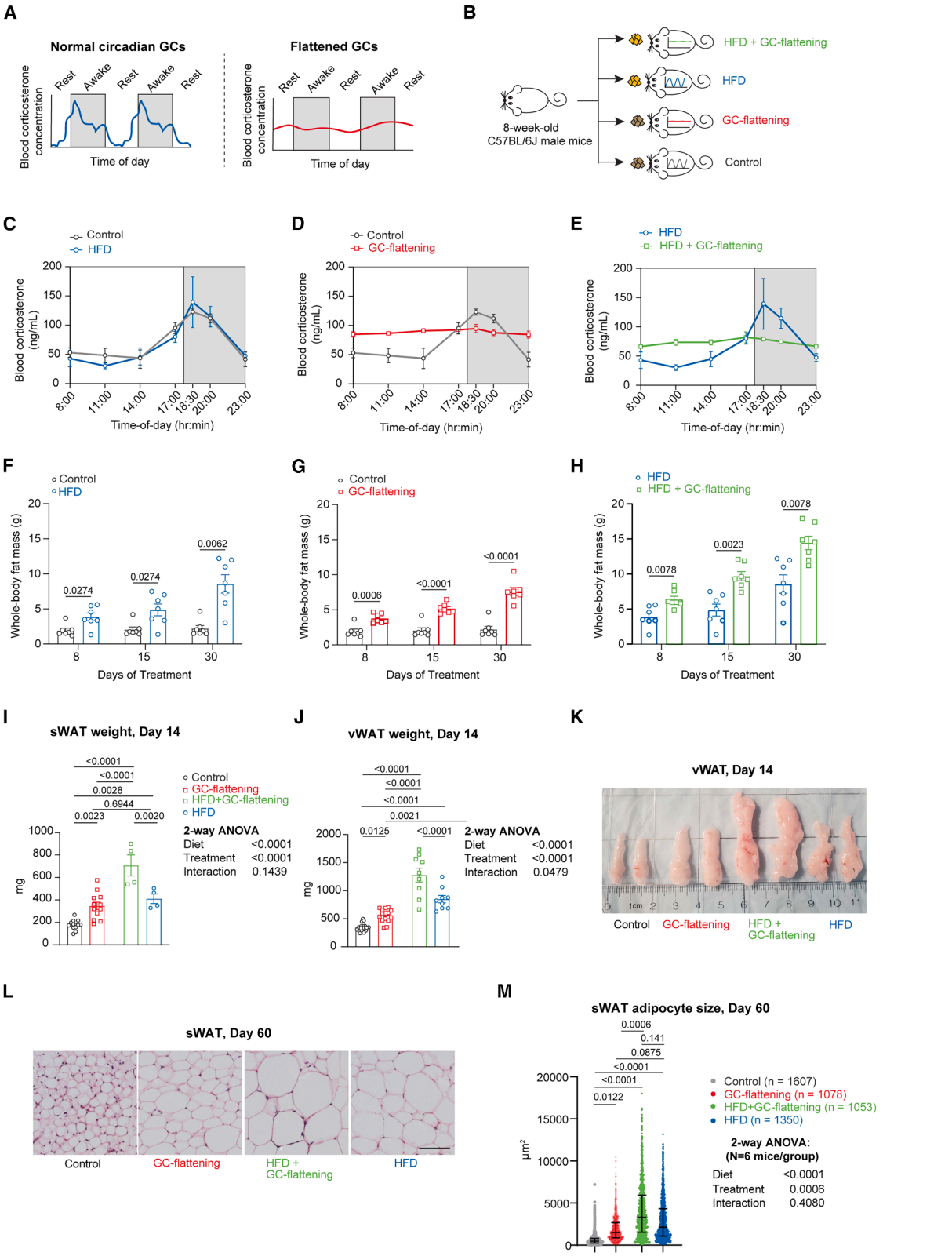

(legend on next page)

which they promote metabolic dysfunction is essential for developing targeted, personalized therapeutic strategies.

In this study, we utilized mouse models to compare the metabolic consequences of obesity induced by GC-flattening versus HFD. We show that while both models reach comparable levels of adiposity, they organize systemic metabolism through fundamentally different architectures. Using gold-standard hyperinsulinemic-euglycemic clamps, we demonstrate that GC-flattening concentrates severe insulin resistance in skeletal muscle. This develops alongside sustained hyperinsulinemia, which allows glucose homeostasis to be maintained despite this resistance. Crucially, this creates a tissue-specific partition. While the muscle is severely resistant, the liver and adipose tissues remain functionally responsive to insulin's suppression of glucose output and lipolysis. This selectivity allows high circulating insulin to effectively suppress lipolysis and hepatic glucose output, thereby sequestering lipids in adipose tissue and protecting the liver from steatosis. Our findings reveal that GC-flattening functionally uncouples obesity from hepatic steatosis, demonstrating that endocrine timing, in addition to total adiposity, is an important determinant of tissue-specific insulin action and systemic metabolic health.

RESULTS

GC-flattening and HFD have additive effects in increasing fat mass

We first determined how GC-flattening and HFD feeding change fat mass over time. To flatten circadian GC rhythms, we implanted mice with pellets that slowly released a low and constant dose of corticosterone, the main physiological GC in mice,[19] over several weeks. We chose the dose of corticosterone to be released such that the mean level of circulating GCs (pellet-released plus endogenous corticosterone) was maintained at normal physiological levels (Figure S1).[10,11,20] This pellet protocol flattens the daily GC rhythm by raising the trough GC level during the rest period and indirectly lowering the peak GC level during the wake period (Figure 1A). This pattern recapitulates the GC-rhythm flattening observed during chronic stress without needing to expose mice directly to a stressor. Thus, the pellet-implantation model allows us to isolate the metabolic consequences of altered GC timing from the many other physiological effects of stress.[6,10–12]

To compare the separate and combined effects of GC-flattening and HFD feeding, we divided 8-week-old C57BL/6J male mice into four treatment groups: (1) chow diet with a placebo pellet (control); (2) chow diet with a corticosterone pellet (GC-flattening); (3) HFD with a placebo pellet (HFD); and (4) HFD with a corticosterone pellet (HFD + GC-flattening) (Figure 1B). Mice were treated for up to 8 weeks. Corticosterone profiles measured at day 52 verified that HFD feeding alone did not alter the circadian GC rhythm (Figure 1C) and confirmed that implanting corticosterone pellets effectively flattened circadian GC rhythms throughout the experimental time frame in both chow- and HFD-fed mice (Figures 1D and 1E), consistent with our previous measurements at day 7 and day 18.[10,11] Mean daily corticosterone levels remained comparable across all groups (Figure S1A). However, GC-flattening caused a modest increase in total daily corticosterone exposure, as measured by the area under the corticosterone curve (Figure S1B), primarily due to elevation of the circadian trough. Thus, the protocol substantially altered hormone timing without producing a large increase in mean circulating corticosterone levels.

Having confirmed that implanting corticosterone pellets flattened GC rhythms consistently throughout the 8-week experimental time frame, we next asked how loss of the oscillatory pattern impacted weight gain and body composition. We employed EchoMRI, a non-invasive technique, to measure changes in whole-body fat mass across the four treatment

Figure 1. GC-flattening and high-fat diet (HFD) have additive effects on increasing fat mass

(A) Glucocorticoids (GCs) are normally secreted in circadian rhythms in healthy mammals, peaking at the start of the active (awake) period and reaching low levels during the rest period. Chronic stress and circadian disruption flatten these rhythms by elevating GC trough levels and blunting daily peaks, while preserving near-normal mean circulating GC concentrations. Corticosterone is the main glucocorticoid in rodents. Shaded regions denote the active (awake) phase.

(B) At day 0, slow-release corticosterone pellets to flatten GC rhythms or placebo pellets were implanted subcutaneously into 8-week-old male C57BL/6J mice, which were then maintained on either a chow diet or HFD. Mice were assigned to four experimental groups: placebo pellet + chow diet (control), corticosterone pellet + chow diet (GC-flattening), placebo pellet + HFD (HFD), and corticosterone pellet + HFD (HFD + GC-flattening).

(C–E) Time course of circulating corticosterone concentrations measured at day 52 of treatment ($n = 5$ mice per group). Shaded regions denote the dark (lights-off) period, during which mice are normally active. The same control cohort is plotted in (C) and (D), and the same HFD cohort in (C) and (E). See also Figure S1.

(F–H) Longitudinal EchoMRI measurements of whole-body fat mass obtained at days 8, 15, and 30 of treatment ($n = 7$ mice per group). Each point represents one mouse. The same control cohort is plotted in (F) and (G), and the same HFD cohort in (F) and (H). See also Figures S2A and S2B for EchoMRI measurements at days 0 and 3 confirming that starting fat mass was equivalent across groups.

(I) Subcutaneous white adipose tissue (sWAT) fat-pad weights measured at day 14 of treatment ($n = 4–12$ mice per group).

(J) Visceral white adipose tissue (vWAT) fat-pad weights measured at day 14 of treatment ($n = 9–17$ mice per group).

(K) Representative images of vWAT depots at day 14 of treatment.

(L) Representative hematoxylin and eosin (H&E)-stained sections of sWAT at day 60. Scale bars, 100 μm.

(M) Distribution of individual sWAT adipocyte cross-sectional areas at day 60, with the median and 25th–75th percentiles indicated. Each point represents one adipocyte ($n = 1,053–1,607$ adipocytes per group; 86–582 per mouse).

Statistical analysis: (C–E) Time-course means and areas under the curve (AUCs) were analyzed using two-way ANOVA as shown in Figure S1. (F–H) At each time point, the two groups shown in each figure were compared by unpaired t test with Welch's correction, using the Holm-Šídák method to correct for comparisons across the three timepoints. Main-effect and interaction statistics for the longitudinal fat-mass data are reported in Figure S2E, which shows the corresponding three-way repeated-measures ANOVA (Time × Diet × Treatment). (I and J) Data were analyzed using two-way ANOVA (Diet × Treatment) with Tukey's post hoc test for multiple comparisons. (M) Per-animal mean adipocyte cross-sectional areas were compared by two-way ANOVA (Diet × Treatment) followed by Tukey's post hoc test, with the animal as the unit of analysis ($n = 6$ mice per group). Individual adipocytes are displayed to show the distribution but were not the unit of statistical analysis. Exact p values are shown within (F)–(J) and (M). Data are presented as mean ± SEM, except in (M), where the median and 25th–75th percentiles are shown.

groups. After confirming that all groups exhibited comparable fat mass at baseline (Figures S2A and S2B), we longitudinally assessed fat mass at 8, 15, and 30 days post-implantation. HFD resulted in a gradual ~3-fold increase in fat mass compared to controls (Figure 1F). Strikingly, despite being on a chow diet, mice subjected to GC-flattening increased fat mass ~2.5-fold, nearly matching the effect of HFD feeding (Figure 1G). Remarkably, the combination of HFD and GC-flattening produced an additive effect, leading to a nearly 5.5-fold increase in fat mass relative to controls (Figure 1H).

Because EchoMRI provides only a whole-body estimate of fat mass and does not distinguish among depots, we dissected mice to isolate and weigh specific white adipose tissue (visceral white adipose tissue [vWAT] and subcutaneous white adipose tissue [sWAT]) depots. These represent the two major anatomical classes of white adipose depots in mammals.[21] Both HFD alone and GC-flattening alone significantly increased vWAT and sWAT weights after 14 days of treatment (Figures 1I–1K). Consistent with the additive effects seen in the EchoMRI data, combining GC-flattening and HFD further increased both sWAT and vWAT weights (Figures 1I and 1J; representative depots in Figures 1K and S3A). The increase was additive for sWAT, with no Diet × Treatment interaction, whereas the two treatments were not fully additive in vWAT (interaction $p = 0.0479$), an early indication of the plateau in vWAT expansion evident at day 60. To assess the durability of these depot-specific effects, we extended the analysis to 60 days. GC-flattening increased sWAT and vWAT weights approximately 3- to 4-fold over control at day 60. Additionally, we observed similar additive effects of GC-flattening and HFD on sWAT (Figures S3B and S3C). However, in mice which underwent GC-flattening on top of an HFD, vWAT weight remained similar to that of mice on HFD alone, suggesting vWAT expansion had plateaued by 60 days (Figures S3D and S3E). This indicates a restricted storage capacity in visceral versus subcutaneous white adipose depots, mirroring human studies that show depot-specific plateaus in lipid turnover during the progression of obesity.[22]

A common feature of HFD-induced obesity is adipocyte hypertrophy, or an increase in the size of individual fat cells. To determine whether GC-flattening also induced hypertrophy, we compared adipocyte size across treatment groups by analyzing paraffin-embedded sWAT sections stained with hematoxylin and eosin (H&E). Adipocyte size greatly increased in mice subjected to either GC-flattening or HFD alone, with a further, largely additive increase when the two treatments were combined (Figures 1L and 1M). We observed similar additive effects on adipocyte hypertrophy in vWAT (Figures S3F and S3G). These histological findings complement our EchoMRI and tissue weight data,supporting that adipocyte hypertrophy is a major contributor to the increase in fat mass under GC-flattening conditions.

Taken together, both GC-flattening and HFD increased adipocyte size and total fat mass. However, HFD increased fat mass through chronic caloric excess without altering circadian GC rhythms (Figures 1C and 1F), while GC-flattening increased fat mass by disrupting GC rhythms in the absence of increased caloric intake (Figures 1D and 1G). These results support that GC-flattening and HFD independently and largely additively promote obesity, producing striking increases in fat mass and adipocyte hypertrophy.

GC-flattening drives lean mass loss despite progressive weight gain

We next examined body weights over time and found that HFD-fed mice became heavier than those subjected to GC-flattening for the same treatment time (Figures 2A and S4). Whereas weight increased immediately and continuously in the HFD-fed mice, the weight gain in the GC-flattened mice was delayed relative to control mice, only increasing after 2 weeks and at a slower rate (Figures 2A and S4). Combining both treatments resulted in an additive increase in weight (Figures 2A and S4). We performed two-way ANOVA to compare the effects of diet and GC-flattening on the body weights measured at day 56. As shown in Figure 2B, while both HFD and GC-flattening each had a significant effect, there was no significant interaction between them in regulating body weights.

The slower rate of body weight gain in the GC-flattened mice was unexpected because the EchoMRI data showed that their fat mass initially increased at a rate similar to the HFD-fed mice. We reasoned that a parallel loss in lean mass could explain the slower body weight gain in GC-flattened mice. Having confirmed that the starting lean mass was consistent across treatment groups, we used EchoMRI and identified a significant reduction in lean mass in GC-flattened mice as early as day 3 (Figures S2C and S2D). The loss in lean mass became more pronounced by day 8 in GC-flattened mice fed either chow (Figure 2E) or HFD (Figure 2F). However, this loss was only transient. After day 8, lean mass in GC-flattened mice stopped declining and began to increase again (Figures 2E, 2F, and S2F). HFD alone did not affect lean mass (Figure 2G). These data demonstrate that HFD increases fat mass without a loss in lean mass. However, GC-flattening increases fat mass while causing an early, transient loss of lean mass (Figures 2C–2E, S2D, and S2F). This explains why GC-flattening results in a smaller overall weight gain than HFD, despite similar increases in adipose tissue mass.

GC-flattening induces selective fast-twitch muscle atrophy

To determine which tissues accounted for the early, acute lean-mass loss observed during GC-flattening, we performed necropsies to dissect and weigh the major lean-mass-contributing organs, which included various skeletal muscles (Figure 2H), as well as the liver, heart, kidneys, and small intestine (Figure S5A). We found that GC-flattening resulted in a selective reduction in the weights of muscles with predominantly fast-twitch fibers—including quadriceps, gastrocnemius, and tibialis anterior (TA), with a comparable but non-significant trend in the extensor digitorum longus (EDL) (Figure 2H). In contrast, the weight of the predominantly slow-twitch oxidative soleus muscle was preserved, indicating that fast-twitch muscles are uniquely sensitive to GC-driven atrophy, consistent with previous studies.[23] Importantly, other major lean organs were unchanged in weight or length (Figure S5A). While we did observe a significant reduction in spleen weight, a stress-associated phenotype consistent with increased GC signaling[24] (Figure S5A), the preservation of other non-skeletal muscle body weights demonstrates that the lean mass deficit primarily reflects selective skeletal muscle atrophy rather than generalized organ wasting.

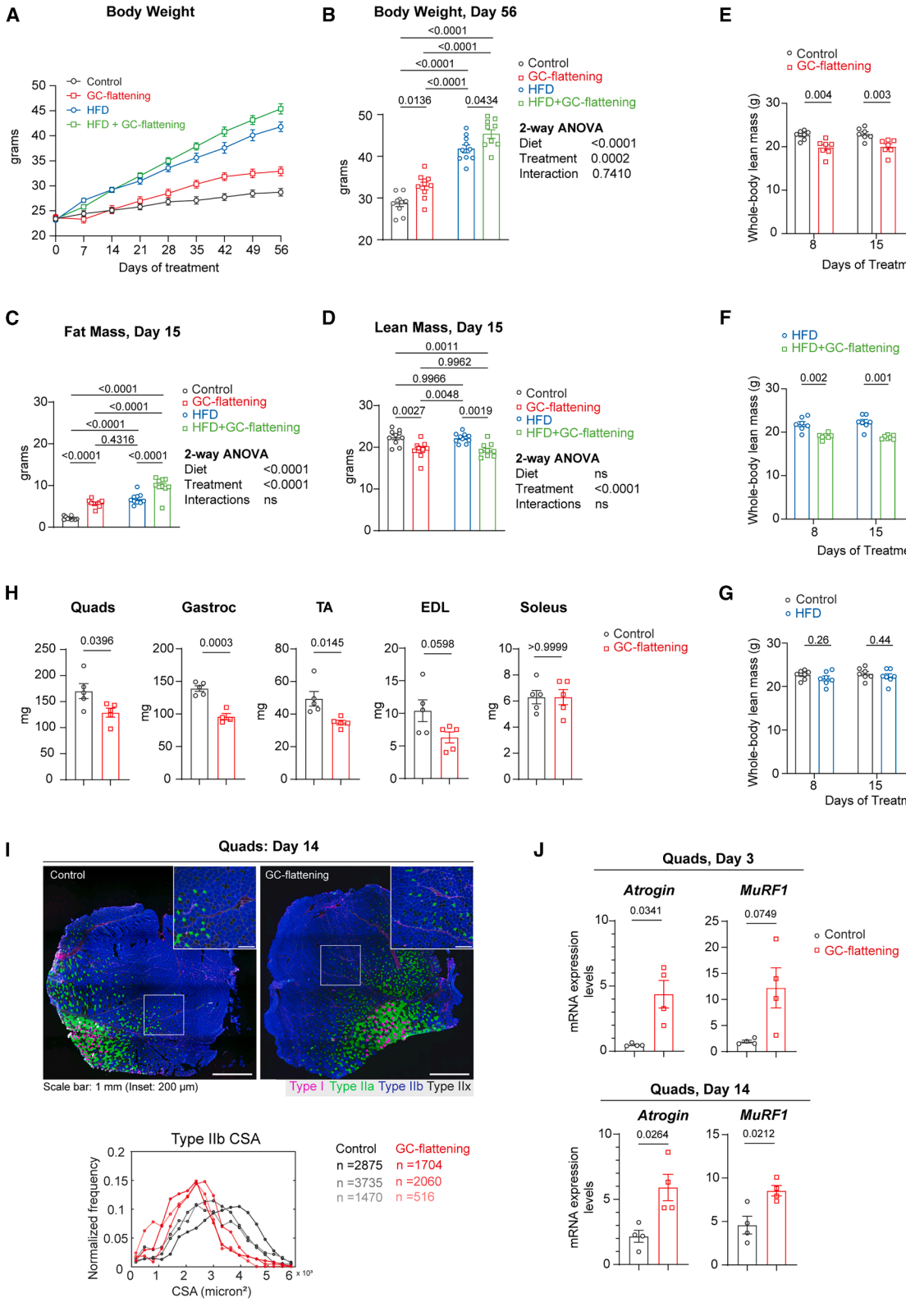

(legend on next page)

We quantified myofiber cross-sectional area (CSA) distributions in two muscles which are enriched in fast-twitch fibers—quadriceps and gastrocnemius—as well as in the predominantly slow-twitch soleus muscle. In quadriceps at day 14, type IIb fibers in GC-flattened mice exhibited a shift toward smaller median CSA, consistent with a reduction in fast-twitch fiber size (Figure 2I). A similar reduction in the size of type IIb fibers was observed in gastrocnemius muscle at day 21 (Figure S5B). In contrast, the size of slow-twitch type I and type IIa fibers in the soleus were largely unchanged under GC-flattening at day 21 (Figure S5B). Together, these data indicate that GC-flattening preferentially targets fast-glycolytic fibers while relatively sparing oxidative slow-twitch populations, consistent with the known susceptibility of type II fibers to GC-induced catabolic signaling.[23]

To determine whether muscle atrophy was accompanied by systemic signatures consistent with enhanced protein turnover, we quantified circulating amino acid levels at early (day 3) and later (day 14) time points. GC-flattened mice exhibited modest but reproducible elevations in several plasma amino acids, including branched-chain and aromatic amino acids (Figure S5C). Although these changes were not uniform across all amino acids, the overall pattern is consistent with increased whole-body protein turnover accompanying GC-induced muscle remodeling.

To define the molecular basis of the fiber-selective atrophy in GC-flattened mice, we quantified the expression of GC-responsive genes in the quadriceps muscle, one of the muscles that experienced significant mass loss during GC-flattening. We found a robust induction of the E3 ubiquitin ligases *Atrogin-1* and *MuRF1*, which are key mediators of ubiquitin-proteasome-dependent muscle atrophy (Figure 2J). Additionally, we observed significant upregulation in other canonical GR target genes and upstream regulators of atrophy, including *FoxO1*, *FoxO3*, *Sesn1*, and *p85*.[25] Notably, while the induction of *p85* was detectable as early as day 3, the activation of the broader *FoxO* transcriptional program became more pronounced and highly significant by day 14 (Figure S5D). These data indicate sustained activation of muscle-intrinsic catabolic signaling pathways under conditions of disrupted GC rhythmicity.

Together, these findings demonstrate that GC-flattening engages a GC-dependent muscle-wasting program that drives early and acute skeletal muscle loss despite substantial adipose expansion. In contrast, HFD-induced obesity markedly increases fat mass while largely preserving lean mass, highlighting that endocrine timing, not adiposity per se, determines whether obesity is accompanied by muscle atrophy.

Sustained hyperinsulinemia induced by GC-flattening suppresses HFD-induced hyperglycemia

Because insulin promotes lipid storage while opposing muscle protein breakdown, the simultaneous gain in fat mass and early loss of lean mass in GC-flattened mice prompted us to examine fasting insulin and glucose. In the classical HFD model, beta cells initially compensate for chronic insulin resistance by increasing insulin secretion. Hyperinsulinemia therefore develops first, and hyperglycemia appears only later, when this compensation fails.[26,27] To determine whether GC-flattening follows this same progression, we compared the time courses of fasting insulin and glucose in the two models. HFD-fed mice showed a gradual rise in fasting insulintogether with an early and sustained increase in fasting glucose (Figures 3A and 3B). In contrast, GC-flattened mice diverged rapidly from this pattern. Fasting insulin rose ~17-fold above controls by day 3 and remained 6- to 7-fold

Figure 2. GC-flattening selectively reduces lean mass and induces fast-twitch muscle atrophy

(A) Time course of absolute body weight (grams) in control, GC-flattened, HFD-fed, and HFD + GC-flattened mice (n = 10 mice per group). See Figure S4 for body-weight gain normalized to each mouse's starting weight.

(B) Body weight at day 56 from (A) illustrating significant weight differences among treatment groups.

(C and D) Body composition assessed by EchoMRI at day 15 showing comparable fat mass between HFD-fed and GC-flattened mice (C) but reduced lean mass specifically in the GC-flattened groups (D) (n = 10 mice per group).

(E–G) Longitudinal EchoMRI measurements of whole-body lean mass obtained at days 8, 15, and 30 of treatment (n = 7 mice per group). See also Figures S2C and S2D for baseline (day 0) and early (day 3) lean-mass measurements, and Figure S2F for the corresponding three-way repeated-measures ANOVA (Time × Diet × Treatment) of the longitudinal lean-mass data.

(H) Skeletal muscle weights measured at day 14 in chow-fed control and GC-flattened mice. GC-flattening caused selective atrophy of glycolytic muscles (quadriceps, gastrocnemius, tibialis anterior, with a comparable but non-significant trend in the extensor digitorum longus), while the predominantly oxidative soleus muscle was preserved. Each data point represents one mouse (n = 5 mice per group). See Figure S5A for weights of other lean mass tissues.

(I) (Top) Representative cross-sections from the quadriceps muscle of control and GC-flattened mice at day 14. The sections were stained with laminin to delineate myofiber boundaries and immunolabeled for myosin heavy-chain isoforms to identify type I, type IIa, and type IIb fiber types. Type IIx fibers were identified by the absence of staining. Type I, type IIa, type IIb, and type IIx are colored in magenta, green, blue, and black, respectively. White boxes indicate regions shown at higher magnification. Scale bars, 1 mm (whole muscle) and 200 μm (zoomed regions). (Bottom) Normalized frequency distributions of myofiber cross-sectional area (CSA) for type IIb fibers. Each curve represents one mouse (n = 3 mice per group). Numbers indicate the total number of fibers analyzed per mouse. See also Figure S5B.

(J) Quantitative PCR analysis of Atrogin-1 and MuRF1 mRNA expression in quadriceps muscle at day 3 and day 14 of GC-flattening, indicating activation of proteolytic pathways. Each data point represents one mouse (n = 4 mice per group).

Statistical analysis: Statistical significance for the body-weight, body-composition, and longitudinal lean-mass data in (A)–(G) was assessed using two-way ANOVA with factors of Diet and Treatment. For (B)–(D), Tukey's post hoc test was used for multiple comparisons, and exact p values for main effects (Diet and Treatment) and their interaction are indicated within the respective figures. The longitudinal lean-mass measurements in (E)–(G) were analyzed by two-way ANOVA with post hoc comparisons at each time point; the p values shown within these figures are for pairwise comparisons, and the corresponding Time × Diet × Treatment analysis is reported in Figure S2F. For the individual muscle weights in (H), statistical comparisons between chow-fed control and GC-flattened groups were performed using two-tailed unpaired t-tests. For the qPCR gene-expression analyses in (J), comparisons were performed using two-tailed unpaired t-tests with Welch's correction. The myofiber cross-sectional area distributions in (I) are shown descriptively. Each curve represents one mouse, and no statistical comparison was performed. All data are presented as mean ± SEM, and exact p values are shown for all statistical comparisons.

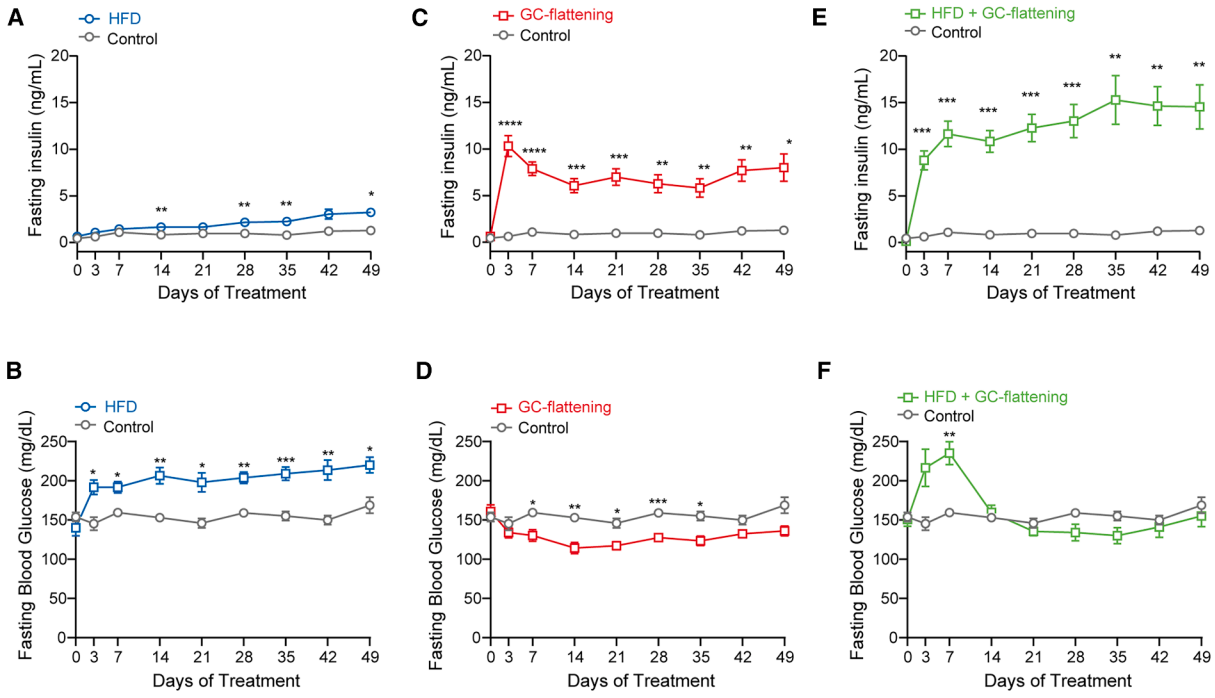

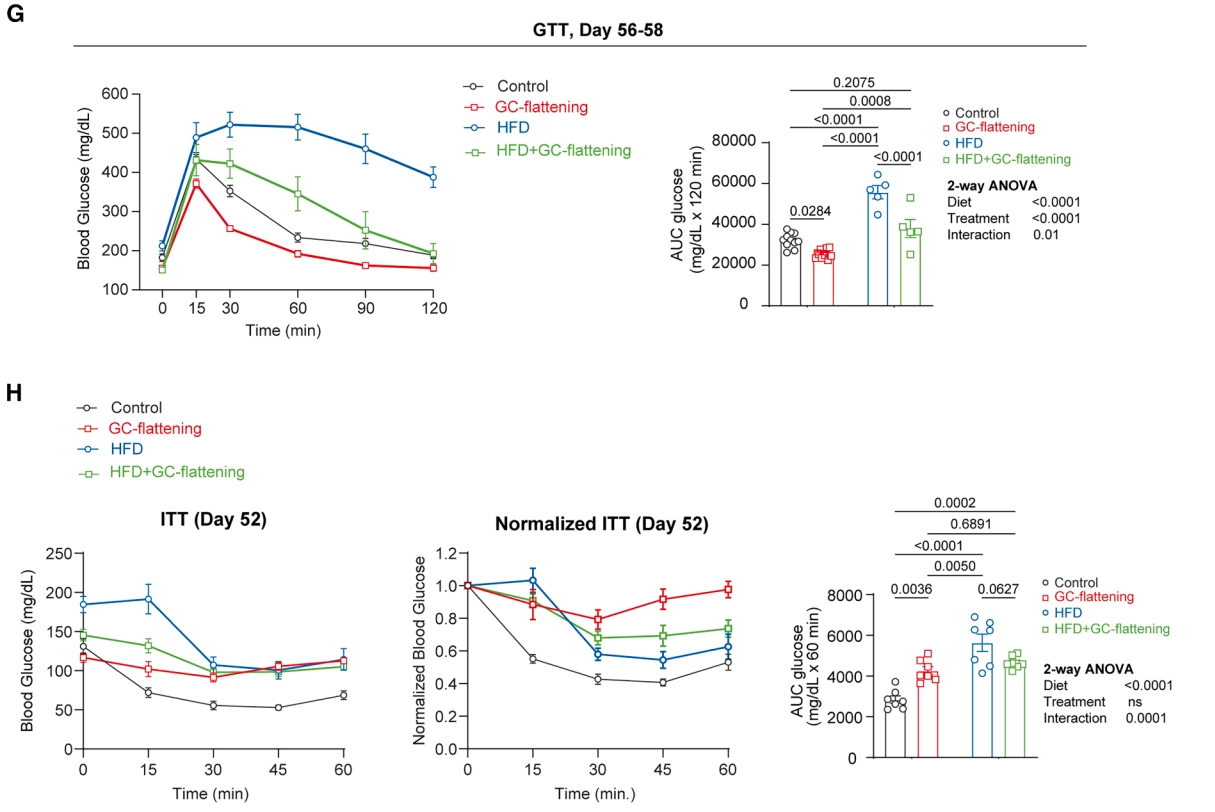

(legend on next page)

elevated throughout the 7-week experiment (Figure 3C) while fasting glucose remained normal (Figure 3D).

The combined GC-flattening + HFD condition provided evidence that the GC-flattening phenotype likely does not represent a transient state preceding beta-cell exhaustion. Under the classical paradigm, the addition of a HFD to an already hyperinsulinemic environment should accelerate the transition to hyperglycemia as beta cells fail to meet the extreme metabolic demand. However, even though combining GC-flattening and HFD resulted in even higher insulin levels than GC-flattening alone (Figure 3E), we did not observe sustained hyperglycemia during the 7-week duration of the experiment. While HFD-fed mice showed the expected steady increase in fasting glucose together with increasing hyperinsulinemia (Figures 3A and 3B), the addition of GC-flattening to HFD-fed mice resulted in a rescue of the hyperglycemia. As shown in Figure 3F, in the HFD + GC-flattening group, the initial increase in blood glucose levels was suppressed by day 14, returning toward control values and remaining generally lower than in mice fed HFD alone for the remaining duration of the experiment.

The observations from the two GC-flattening treatment groups highlight a critical divergence from the beta-cell exhaustion model. In the GC-flattened mice, either fed chow or HFD, insulin levels reach a massive, stable plateau almost immediately and stay at high levels (Figures 3C and 3E), yet the mice exhibit sustained normoglycemia (albeit slightly lower than control levels) rather than developing hyperglycemia as predicted by the classical model. The sustained hyperinsulinemia together with normalization of blood glucose by day 14 suggests that GC-flattening produces a strong increase in circulating insulin that is sufficient to counteract the hyperglycemic effects of HFD. However, the mechanism by which GC-rhythm flattening produces the sustained hyperinsulinemia remains to be determined.

GC-flattening enhances glucose tolerance despite systemic insulin resistance

We next sought to understand why fasting glucose levels are lower in GC-flattened mice compared to HFD-fed mice. We hypothesized that the persistent hyperinsulinemia in GC-flattened mice might lead to more effective glucose disposal or more robust suppression of endogenous glucose production compared to HFD-fed mice. To test for enhanced glucose tolerance, we performed glucose tolerance tests (GTTs) and insulin tolerance tests (ITTs) in mice subjected to GC-flattening, HFD feeding, or a combination of both treatments. Measurements were conducted after 8 weeks to allow sufficient time for the effects of HFD feeding to manifest.

GTT time courses and AUC calculations revealed that GC-flattened mice exhibited significantly accelerated glucose clearance compared to control mice (Figure 3G). This enhanced clearance likely results from the profound basal hyperinsulinemia present in GC-flattened mice prior to the glucose challenge (Figure 3C). As expected, the HFD-fed mice exhibited impaired glucose clearance. Interestingly, GC-flattening on top of HFD improved glucose clearance compared to HFD alone (Figure 3G). These GTT results collectively demonstrate that GC-flattening improved glucose tolerance in both control and HFD-fed mice.

To assess peripheral insulin sensitivity, we performed ITTs by injecting insulin into the mice and measuring the rate of blood glucose decline. While control mice showed a rapid decline in blood glucose within 30 min of insulin injection, HFD-fed mice exhibited a significantly blunted response, indicative of diet-induced insulin resistance (Figure 3H). Strikingly, despite having better glucose tolerance, GC-flattened mice displayed worse insulin sensitivity than control mice, as demonstrated by their inability to lower blood glucose levels as effectively after insulin injection (Figure 3H). Notably, the insulin-resistant response was comparable in GC-flattened mice on either diet, although the effect of GC-flattening reached significance only on the chow background (Figure 3H). Overall, the GTT and ITT results show that disruption of GC rhythms induces marked systemic insulin resistance, yet surprisingly, this resistance is associated with improved glucose tolerance.

GC-flattening induces a sustained hyperinsulinemic state

The GTT and ITT results present a metabolic paradox: GC-flattened mice show improved glucose tolerance but are significantly insulin resistant. To resolve this contradiction, we utilized the hyperinsulinemic-euglycemic clamp, the gold standard for quantifying *in vivo* insulin sensitivity.[28,29] Unlike the ITT, which relies on a single insulin bolus that can trigger confounding counter-regulatory hormone responses, the clamp technique allows for the maintenance of constant, controlled insulin levels throughout the experimental period, providing a more precise measure of insulin sensitivity[28,29] (Figures 4A and 4B).

Figure 3. GC-flattening rapidly induces marked hyperinsulinemia while maintaining fasting glucose and improving glucose tolerance

(A, C, and E) Fasting Insulin: measured over 7 weeks in control, HFD-fed, GC-flattened, and HFD + GC-flattened mice. GC-flattening induced an early, several-fold elevation in fasting insulin that exceeded the modest increase produced by HFD alone (n = 10 mice per group).

(B, D, and F) Fasting Glucose: measured longitudinally in the same mice shown in (A, C, and E). Despite pronounced hyperinsulinemia, GC-flattened mice maintained fasting glucose at or slightly below control levels, whereas HFD-fed mice developed progressive hyperglycemia.

(G) Glucose Tolerance Test (GTT): performed on days 56–58 of treatment. Blood glucose concentrations were measured following glucose administration (left), and the corresponding area under the curve (AUC) was calculated (right). GC-flattening enhances glucose tolerance in both chow- and HFD-fed backgrounds. Control, n = 11; GC-flattening, n = 11; HFD, n = 5; HFD + GC-flattening, n = 5.

(H) Insulin Tolerance Test (ITT): performed on day 52 of treatment. Blood glucose was measured following insulin administration and is presented as both absolute concentrations (left) and normalized to initial fasting glucose (middle). The corresponding AUC is shown on the right. The ITT demonstrates systemic insulin resistance induced by GC-flattening, which reached significance on the chow background. n = 7 mice per group.

Statistical analysis: data in (A)–(F) were analyzed using two-way repeated-measures ANOVA with Šídák's correction. The AUC values in (G) and (H) were analyzed using two-way ANOVA (Diet × Treatment) with Tukey's post hoc test. The p values for main effects and interactions are indicated within the figures. In (A)–(F), $^{*}p < 0.05$, $^{**}p < 0.01$, $^{***}p < 0.001$, $^{****}p < 0.0001$, ns = not significant. Exact p values for key comparisons are shown. All data are presented as mean ± SEM.

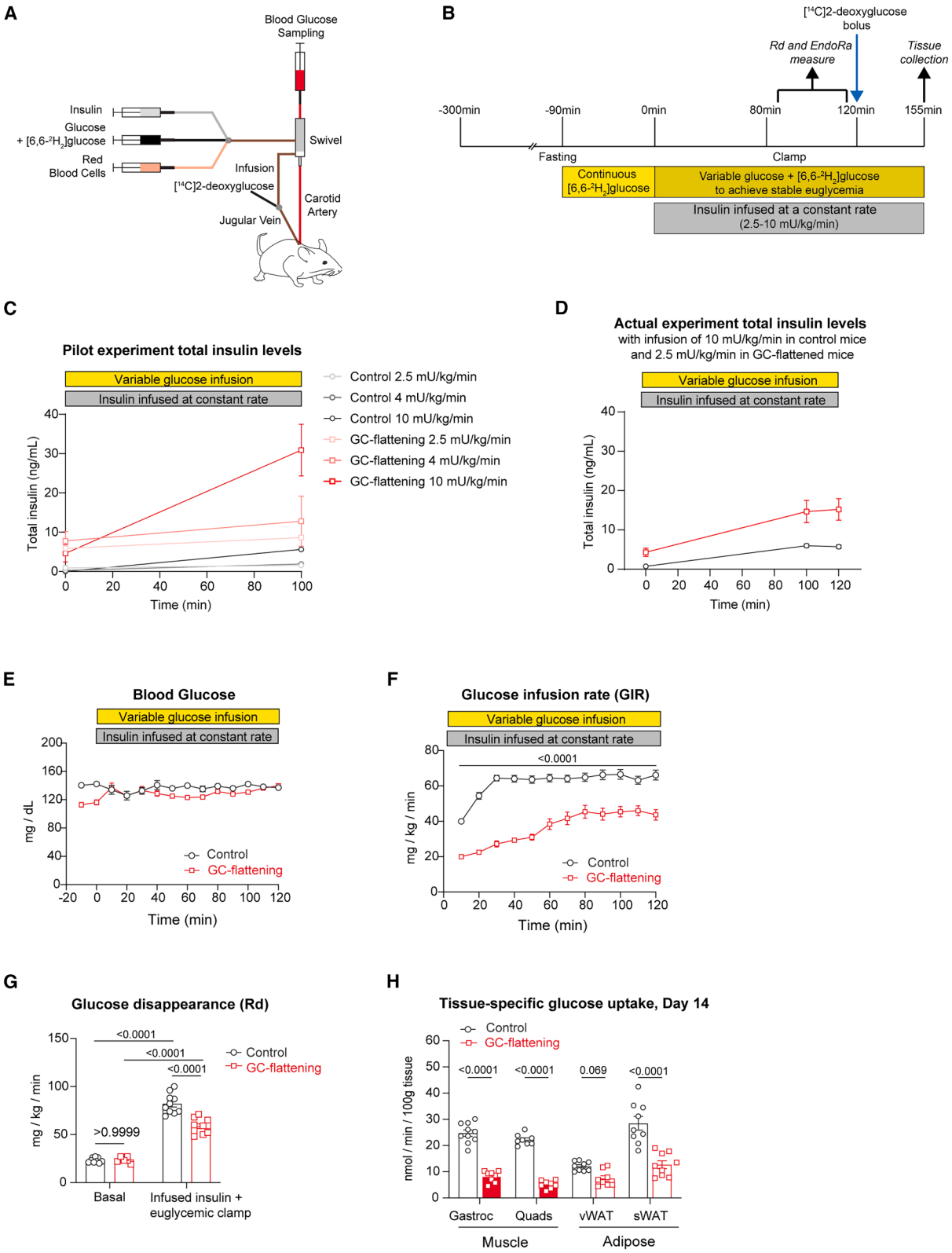

(legend on next page)

Because the GC-flattened mice maintain significantly higher endogenous insulin levels than controls, we first conducted pilot experiments to identify infusion rates that would reduce differences in total circulating insulin levels between GC-flattened and control mice. We infused three different doses of insulin (2.5, 4, and 10 mU/kg/min) and measured the resulting total circulating insulin (sum of the infused plus endogenous circulating insulin; Figure 4C). For the actual experiment, we used an infusion rate of 2.5 mU/kg/min for the GC-flattened mice and 10 mU/kg/min for the control mice since the latter dose was the highest we could safely infuse into the control mice without any unexpected toxic effects. Notably, the total insulin levels were greatly elevated in the control mice at the 10 mU/kg/min infusion rate but remained lower than the concentrations achieved in GC-flattened mice receiving only 2.5 mU/kg/min (Figure 4D).

While insulin was infused at these constant rates, glucose was co-infused at the rates necessary to maintain euglycemia (~140 mg/dL; Figure 4E). Lower glucose infusion rate (GIR) corresponds to increased insulin resistance, and the GIR in the GC-flattened mice was approximately two-thirds that of the control mice (Figure 4F), despite their higher total circulating insulin (Figure 4D). The Rd value reflects the rate of glucose disappearance from the bloodstream and thus corresponds to whole-body tissue glucose uptake. Despite their profound insulin resistance, GC-flattened mice remained capable of effective glucose clearance, as evidenced by a significant increase in Rd when transitioning between basal and clamped conditions (Figure 4G). Collectively, these data demonstrate that GC-flattening induces a state in which elevated insulin maintains euglycemia despite severe insulin resistance. This contrasts to diet-induced obesity (DIO) models in which hyperglycemia develops because insulin secretion fails to match the degree of insulin resistance.

GC-flattening redistributes insulin resistance across tissues, concentrating signaling defects in skeletal muscle

To investigate whether tissue-specific differences in insulin-mediated glucose uptake account for this unique metabolic profile, we compared insulin-stimulated glucose disposal across various tissues. During the insulin-clamp experiments, we injected a bolus of radiolabeled glucose ([^{14}C]2-deoxyglucose, blue arrow, Figure 4B). Mice were sacrificed 35 min later, and tissues were collected to determine how much radiolabeled glucose was incorporated. We found that insulin-stimulated glucose uptake was significantly reduced in skeletal muscle (gastrocnemius and quadriceps) and in sWAT, with a non-significant reduction in vWAT (Figure 4H), indicating impaired insulin-stimulated glucose uptake in both muscle and adipose tissue.

To identify the molecular mechanisms underlying the reduced glucose uptake, we measured components of the canonical insulin-signaling pathway in the key metabolic tissues. In skeletal muscle, we analyzed insulin receptor abundance (IRβ) alongside key downstream nodes, including the PI3K regulatory subunit p85, a negative regulator of muscle insulin signaling[30] that is transcriptionally controlled by glucocorticoid receptor (GR) signaling,[25] and insulin-stimulated AKT phosphorylation (Figures 5A–5H). GC-flattening resulted in molecular changes that were consistent with reduced insulin-mediated glucose uptake in skeletal muscle. Specifically, in the quadriceps, the levels of p85 were significantly elevated already by day 3 and remained high at day 21 (Figures 5A and 5B). IRβ abundance was significantly reduced at day 14 through day 21 (Figures 5A and 5C), and AKT phosphorylation

Figure 4. Hyperinsulinemic-euglycemic clamp studies reveal severe systemic insulin resistance with substantial glucose disposal maintained by hyperinsulinemia

Measurements were performed in chow-fed control and GC-flattened mice after 14 days of treatment. n = 8–11 mice per condition, except where noted.

(A) Schematic of the dual-catheter infusion and sampling setup. Insulin, glucose, and [6,6-$^{2}H_2$]glucose were infused via the jugular vein, while blood samples were collected from the carotid artery for glucose and tracer measurements. A bolus of [^{14}C]2-deoxyglucose was administered to assess tissue-specific glucose uptake.

(B) Timeline of the clamp protocol. Following a fasting period, a continuous infusion of [6,6-$^{2}H_2$]glucose was initiated for 90 min to enrich plasma glucose isotopically. A hyperinsulinemic-euglycemic clamp was then performed using a constant-rate insulin infusion with variable glucose infusion to maintain euglycemia at ~140 mg/dL. Rates of glucose disappearance (Rd) and endogenous glucose production (EndoRa) were measured during the steady-state period. A bolus of [^{14}C]2-deoxyglucose was administered at 120 min during the clamp to assess tissue glucose uptake, followed by tissue collection 35 min later (155 min total). Heparinized, saline-washed donor erythrocytes were infused throughout to maintain hematocrit.

(C) Pilot experiment used to select insulin infusion rates that would reduce differences in total circulating insulin levels between groups. Control and GC-flattened mice received increasing insulin doses (2.5–10 mU/kg/min) to identify infusion rates that minimized differences in total plasma insulin concentrations between groups. n = 2–3 mice per dose.

(D) Total plasma insulin levels in the actual clamp experiments, measured before insulin infusion (0 min) and during the clamp (100 and 120 min). Because of their elevated endogenous insulin levels, GC-flattened mice were infused at a lower insulin rate (2.5 mU/kg/min) than controls (10 mU/kg/min). Despite the lower infusion rate, total plasma insulin remained higher in GC-flattened mice during the clamp.

(E) Blood glucose during clamps. Arterial glucose remained at target euglycemia (~140 mg/dL) in both groups throughout the first 120 min of the insulin infusion.

(F) Glucose infusion rate (GIR) required to maintain euglycemia. GC-flattened mice required a significantly lower GIR ($p < 0.0001$), indicating reduced whole-body insulin sensitivity.

(G) Whole-body glucose disappearance (Rd). Basal Rd was similar between control and GC-flattened mice. During the clamp, Rd increased in both groups but was lower in GC-flattened mice than in control mice. Although the lower GIR in GC-flattened mice confirms systemic insulin resistance, the substantial Rd maintained during the clamp indicates that their marked hyperinsulinemia compensates for this resistance and sustains whole-body glucose disposal.

(H) Tissue-specific glucose uptake at day 14 measured 35 min after the [^{14}C]2-deoxyglucose bolus. GC-flattened mice show significantly reduced insulin-stimulated uptake in skeletal muscle (Gastroc and Quads) and in sWAT, with a non-significant reduction in vWAT. All clamp-based glucose-uptake measurements were performed during the rest (light) period. Tissue comparisons are therefore restricted to this circadian phase.

Statistical analysis: For (E)–(G), data were analyzed using two-way repeated-measures ANOVA with Šídák's test for multiple comparisons. (H) was analyzed using two-way ANOVA with Šídák's test. Exact p values are indicated within the figures. All data represent mean ± SEM.

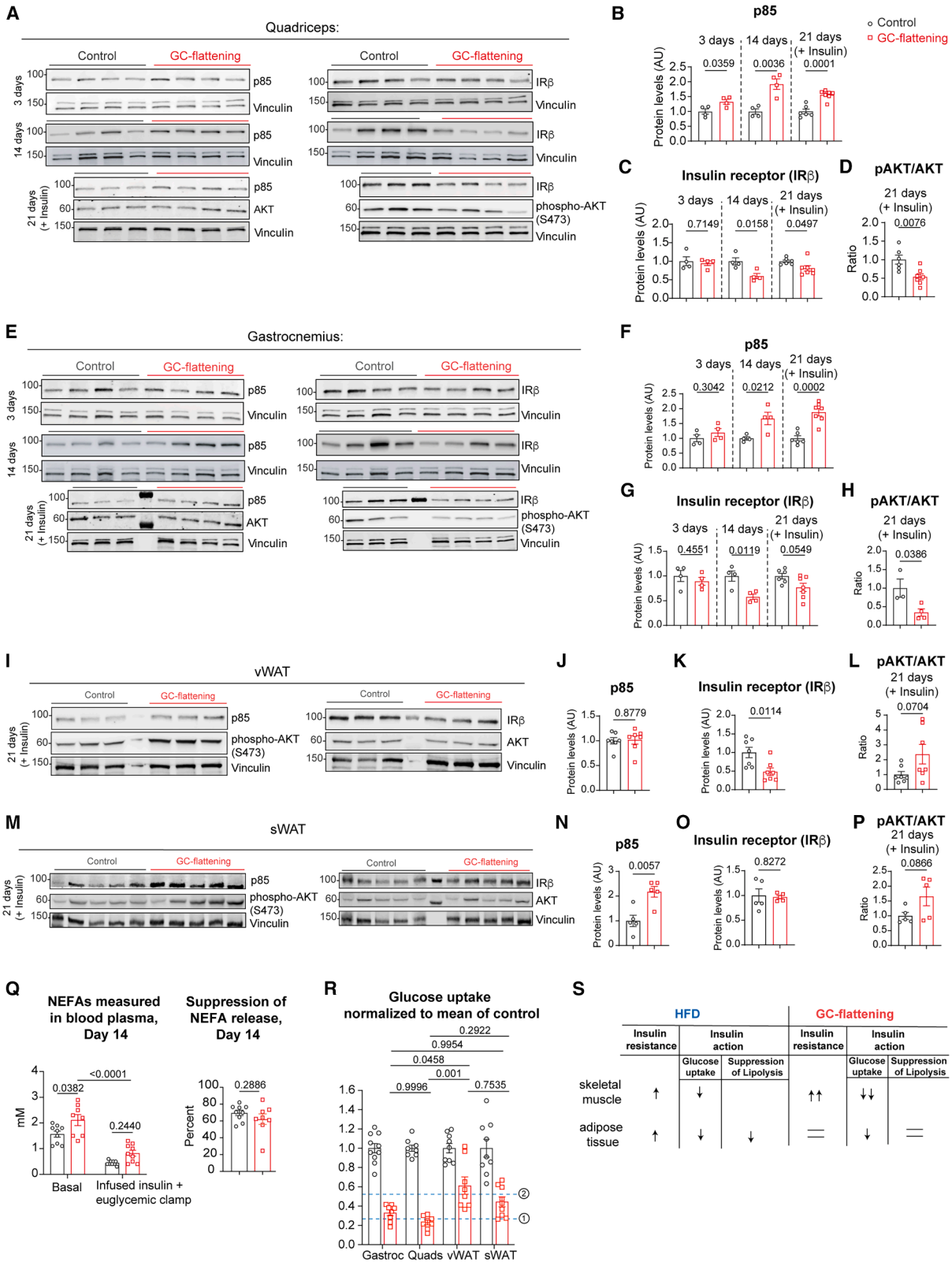

(legend on next page)

(Ser473) was significantly reduced following insulin stimulation at day 21 (Figures 5A and 5D). A similar pattern was observed in gastrocnemius muscle, where the levels of p85 and IRβ were significantly increased and reduced, respectively, by day 14 (Figures 5E, 5F, and 5G), and AKT phosphorylation (Ser473) was significantly reduced following insulin stimulation at day 21 (Figure 5H).

In striking contrast to the coordinated insulin signaling impairment observed in skeletal muscle, adipose tissue exhibited a heterogeneous response. Western blot analysis of vWAT and sWAT revealed depot-specific alterations, such as decreased IRβ abundance in vWAT and increased p85 in sWAT, which were indicative of localized insulin resistance (Figures 5I–5K and 5M–5O). However, unlike the profound downregulation of pAKT signaling in skeletal muscle (Figures 5D and 5H), insulin-stimulated AKT phosphorylation was preserved in both vWAT and sWAT (Figures 5L and 5P). Thus, while GC-flattening induces systemic insulin resistance, the molecular consequences differ sharply between skeletal muscle and adipose tissue, with skeletal muscle showing coordinated impairment of insulin signaling and adipose tissue showing more limited, depot-specific alterations without loss of downstream AKT activation (Figures 5D, 5H, 5L, and 5P).

Functional insulin action is preserved in adipose tissue despite systemic insulin resistance

To determine if the divergent signaling patterns observed in western blotting translated to functional metabolic differences, we assessed tissue-specific insulin action *in vivo*. First, to assess adipose tissue insulin function, we measured plasma non-esterified fatty acid (NEFA) levels during the hyperinsulinemic-euglycemic clamps to readout the ability of insulin to suppress adipose tissue lipolysis (Figure 5Q). Basal NEFA levels were modestly elevated in GC-flattened mice ($p = 0.038$), consistent with the increased adipose mass in these animals. We found that despite whole-body insulin resistance, GC-flattened mice exhibited robust insulin-mediated suppression of NEFA release, with circulating levels dropping to concentrations not significantly different from controls ($p = 0.24$), and percent suppression did not differ significantly between groups ($p = 0.29$), supporting that this key action of insulin was intact in the adipose tissue (Figure 5Q).

To compare insulin-mediated glucose uptake in adipose and muscle tissues *in vivo*, we normalized the tracer-based glucose uptake previously presented in Figure 4H, such that absolute glucose uptake levels in each tissue of GC-flattened mice were normalized to the mean glucose uptake within the same tissue of control mice. This analysis showed that GC-flattening reduced insulin-stimulated glucose uptake in all four tissues, but not equally: gastrocnemius and quadriceps retained only ∼33% and ∼23% of control uptake, compared with ∼61% in vWAT and ∼45% in sWAT. Uptake in both muscles was significantly lower than in vWAT (Figure 5R), with sWAT intermediate.

Taken together, these data suggest that GC-flattening selectively partitions functional resistance to the skeletal muscle. Unlike standard DIO, which impairs insulin action across muscle and adipose tissues simultaneously, GC-flattening impairs muscle glucose uptake more severely than in adipose tissue, which remains responsive to insulin-mediated suppression of lipolysis and retains insulin-stimulated AKT phosphorylation (Figures 5Q and 5S).

GC-flattening uncouples profound obesity from pathological hepatic steatosis

In typical DIO, adipose tissue insulin resistance triggers the uncontrolled release of NEFAs, driving ectopic lipid accumulation

Figure 5. GC-flattening impairs insulin signaling in skeletal muscle but preserves insulin-stimulated AKT phosphorylation and insulin action in adipose tissue

(A–D) Quadriceps: (A) Representative immunoblots of p85, insulin receptor β (IRβ), phospho-AKT (Ser473), total AKT, and vinculin in quadriceps from control and GC-flattened mice at days 3, 14, and 21. (B–D) Quantification of p85 (B) and IRβ (C) at days 3, 14, and 21, and of phospho-AKT (Ser473) relative to total AKT at day 21 (D).

(E–H) Gastrocnemius: the same measurements in gastrocnemius muscle: immunoblots (E), p85 (F), IRβ (G), and pAKT/AKT at day 21 (H).

Day 3 and day 14 samples were collected under basal conditions; day 21 samples were collected 10 min after intraperitoneal injection of insulin (5 U/kg body weight) following a 5-h fast. $n = 4$ mice per group at days 3 and 14 and $n = 6–7$ at day 21, except in (H), where $n = 3–4$.

(I–L) Visceral white adipose tissue (vWAT): representative immunoblots (I) and quantification of p85 (J), IRβ (K), and pAKT/AKT (L) at day 21 following insulin stimulation ($n = 7$ mice per group).

(M–P) Subcutaneous white adipose tissue (sWAT): representative immunoblots (M) and quantification of p85 (N), IRβ (O), and pAKT/AKT (P) at day 21 following insulin stimulation ($n = 5$ mice per group).

(Q) Left: plasma non-esterified fatty acids (NEFAs) at day 14 under basal conditions and during hyperinsulinemic-euglycemic clamps. Right: percent suppression of plasma NEFA levels during clamps at day 14 ($n = 8–9$ mice per group).

(R) Comparison of insulin-stimulated glucose uptake across tissues, normalized to the mean of each tissue's respective control ($n = 8–10$ mice per group). All clamp-based glucose-uptake measurements were performed during the rest (light) period; tissue comparisons are therefore restricted to this circadian phase. See also Figure 4H for the corresponding un-normalized tissue-specific glucose uptake.

(S) Summary Table: comparative overview of insulin resistance and action in skeletal muscle and adipose tissue under high-fat diet (HFD) versus GC-flattening conditions. HFD is known to induce insulin resistance in both skeletal muscle and adipose tissue (↑). This manifests as reduced glucose uptake in both tissues and an inability to suppress lipolysis in the adipose tissue (↓). In contrast, GC-flattening causes severe insulin resistance in skeletal muscle, whereas adipose tissue shows more limited and heterogeneous signaling alterations with preserved insulin-stimulated AKT phosphorylation. Glucose uptake is also more severely impaired in the muscle compared to adipose tissue (↓↓ vs. ↓). Suppression of lipolysis in response to insulin further supports that GC-flattening preserves insulin action in the adipose tissue (=).

Statistical Analysis: vinculin served as the loading control for all representative immunoblots. Statistical significance for individual protein abundance (B–D, F–H, J–L, and N–P) and for percent NEFA suppression (Q, right) was assessed using two-tailed unpaired *t* tests. For the basal versus clamp NEFA concentrations (Q, left) and the tissue-specific glucose uptake (R), statistical significance was determined by two-way ANOVA followed by Šídák's multiple comparisons test. For (R), glucose uptake in each tissue was normalized to the corresponding control mean for that tissue, and the *p* values shown are for comparisons among the GC-flattened groups. Exact *p* values are indicated within the figures, and all data are presented as mean ± SEM.

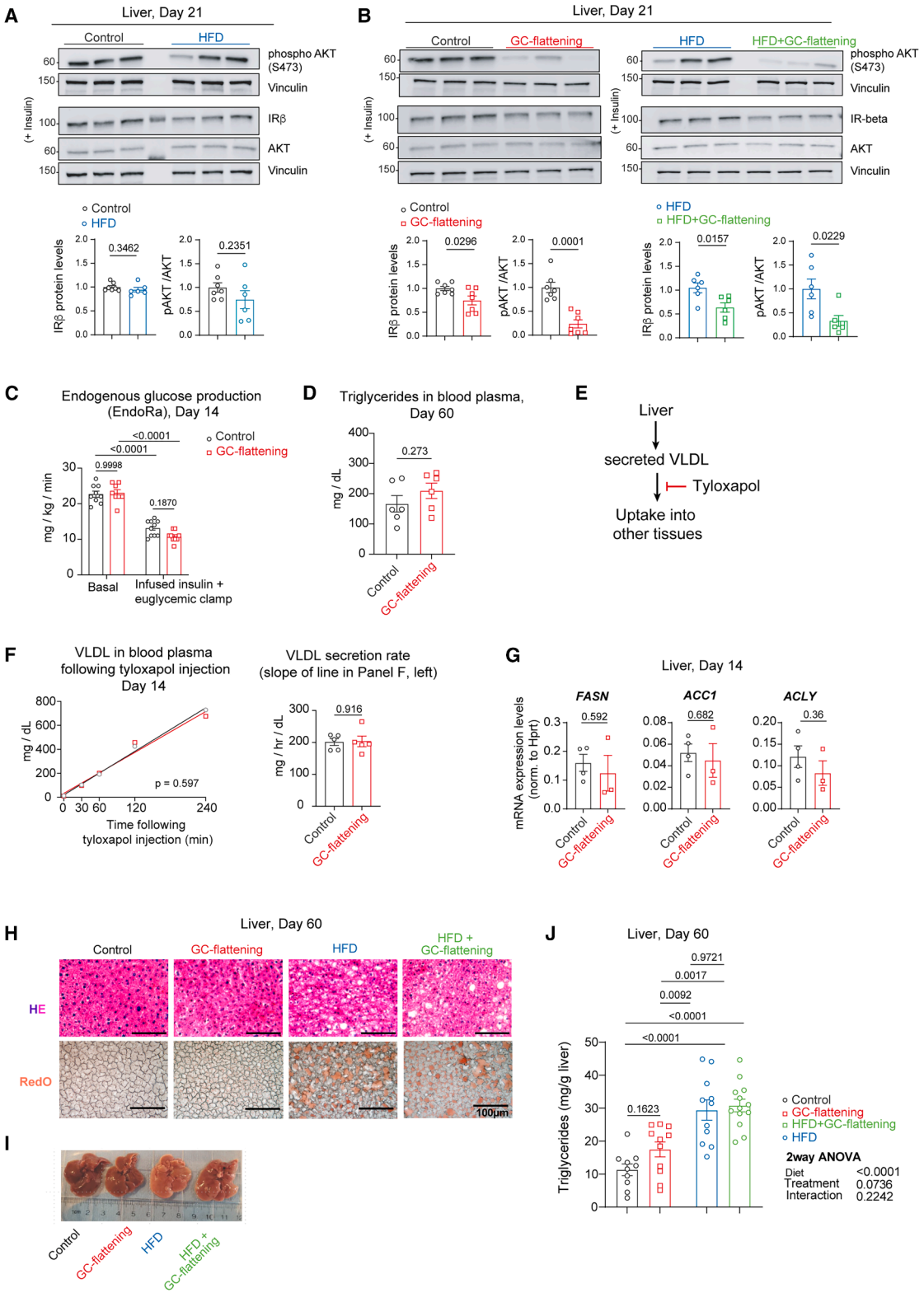

(legend on next page)

in the liver. However, despite profound obesity and systemic insulin resistance, GC-flattened mice maintain insulin-mediated suppression of NEFA release (Figure 5Q), limiting the flux of lipotoxic fatty acids to the liver. To determine the functional consequences of this preserved adipose-liver axis, we examined hepatic insulin signaling and lipid homeostasis (Figure 6).

Western blot analysis of liver tissue at day 21 showed that livers of HFD-fed mice largely maintain insulin signaling as insulin receptor (IRβ) abundance was unchanged and no significant changes were observed in insulin-stimulated AKT phosphorylation (Figure 6A). In contrast, GC-flattened livers, under both chow and HFD conditions, already exhibited a reduction in IR abundance and a corresponding decrease in insulin-stimulated AKT phosphorylation (Figure 6B). Notably, a longitudinal comparison of Western blots at 21 and 60 days (Figures 6A, 6B, and S6A–S6C) demonstrates that these molecular signaling defects emerge earlier in GC-flattened mice than in HFD-fed mice, where signaling typically remains intact during the initial phases of weight gain.[31] Because the day 21 and day 60 immunoblots used different insulin doses (5 and 0.75 U/kg, respectively), absolute phosphorylation levels are not comparable across time points. Treatment effects were therefore assessed within each time point against controls receiving the identical dose.

However, consistent with observations in adipose tissue (Figure 5), this early downregulation of signaling components in GC-flattened mice did not manifest as functional metabolic failure. This stands in sharp contrast to standard HFD-induced progression, where functional metabolic failure typically precedes detectable defects in the cellular insulin signaling pathway.[31] Hyperinsulinemic-euglycemic clamp studies confirmed that insulin-mediated suppression of endogenous glucose production by the liver was preserved in GC-flattened mice (Figure 6C). Because endogenous glucose production is governed by several counter-regulatory inputs in addition to insulin—including glucagon and growth hormone—we interpret this result as preserved hepatic insulin responsiveness rather than as a direct readout of GC signaling. This functional sensitivity was further supported by gene expression data at day 60; mRNA levels of key gluconeogenic enzymes (*Pepck1*, *Pepck2*, and *G6pc*) remained at baseline in GC-flattened mice (Figure S6D), with no evidence of the runaway gluconeogenesis typically seen in hepatic insulin resistance.

Interestingly, the liver was largely protected from many of the adverse metabolic signatures that usually accompany increased adiposity in HFD mice. Plasma triglyceride levels were not overtly elevated in GC-flattened mice, although a non-significant trend toward an increase was observed (Figure 6D). To directly assess hepatic lipid output, we measured the very-low-density lipoprotein (VLDL) secretion rate by monitoring plasma triglyceride accumulation following injection of tyloxapol, a lipoprotein lipase inhibitor that blocks intravascular triglyceride hydrolysis and peripheral clearance of triglyceride-rich lipoproteins (Figure 6E). We found that neither circulating triglyceride concentrations over time (Figure 6F, left) nor the calculated VLDL secretion rate (Figure 6F, right) differed significantly between control and GC-flattened mice. This preservation of normal lipid export was further supported by gene expression data, as mRNA levels of key *de novo* lipogenesis enzymes (Fasn, Acc1, and Acly) remained at baseline (Figure 6G).

Hepatic health was analyzed by morphological and biochemical analysis at day 60. Gross morphology and histological assessment via H&E and Oil Red O staining revealed minimal lipid deposition in GC-flattened livers, standing in sharp contrast to the extensive macrovesicular steatosis observed in HFD-fed mice (Figures 6H and 6I). Quantification of liver triglycerides showed no significant difference between control and GC-flattened mice, and levels remained markedly lower than in HFD-fed mice (Figure 6J).

These data indicate that the early molecular downregulation of hepatic insulin signaling does not translate to a loss of metabolic

Figure 6. GC-flattening uncouples profound obesity from pathological hepatic steatosis

(A) Hepatic Insulin Signaling in HFD-fed Mice: representative immunoblots and quantification of IRβ abundance and phospho-AKT (Ser473) relative to total AKT in insulin-stimulated liver lysates from control and HFD-fed mice at day 21. Neither IRβ abundance nor the pAKT/AKT ratio differs between groups.

(B) Hepatic Insulin Signaling in GC-flattened Mice: the same measurements in control versus GC-flattened mice (left) and in HFD versus HFD + GC-flattened mice (right) at day 21. GC-flattening reduces IRβ abundance and insulin-stimulated AKT phosphorylation on both chow and HFD backgrounds.

For (A and B), mice were fasted for 5 h, and tissues were collected 10 min after intraperitoneal insulin injection (5 U/kg body weight). Each group pair was run on a separate blot and compared independently. Vinculin was used as the loading control (n = 6–7 mice per group).

(C) Endogenous Glucose Production (EndoRa): measured at day 14 under basal conditions (−10 min) and during the hyperinsulinemic-euglycemic clamp (average of 80–120 min). Insulin suppresses endogenous glucose production in GC-flattened mice to a degree comparable to controls (n = 8–10 mice per group).

(D) Plasma Triglycerides: circulating levels measured at Day 60 (n = 6 mice per group).

(E and F) VLDL Secretion Assay: (E) Schematic of the tyloxapol-based VLDL secretion assay. (F) Plasma triglycerides over time following tyloxapol injection at day 14 (left) and calculated VLDL secretion rates (right) (n = 5 mice per group).

(G) *De Novo* Lipogenesis: hepatic expression of lipogenic genes (Fasn, Acc1, and Acly) at day 14 (n = 3–4 mice per group). All gene expression analysis was performed from tissues collected during the rest (light) period, when hepatic lipogenesis is typically low in mice.

(H) Liver Histology: representative H&E and Oil Red O-stained liver sections at day 60. GC-flattened mice show minimal hepatic lipid accumulation compared with extensive macrovesicular steatosis in HFD-fed mice. Scale bars, 100 μm.

(I) Gross Morphology: liver appearance at day 60. Livers from GC-flattened and HFD + GC-flattened mice maintain a normal overall appearance, whereas HFD livers are enlarged and overtly steatotic.

(J) Hepatic Triglyceride Content: quantitative measurement at day 60. Liver triglyceride levels did not differ significantly between control and GC-flattened mice and remained far below those observed in HFD-fed mice (n = 10–13 mice per group).

Statistical Analysis: for (A) and (B) statistical significance was assessed using two-tailed unpaired t tests. For (D), (F, right), and (G), statistical significance was assessed using two-tailed unpaired t tests with Welch's correction. For (C), significance was determined by two-way ANOVA (Treatment × Condition) followed by Tukey's post hoc test for multiple comparisons. For (J), significance was determined by two-way ANOVA (Diet × Treatment) followed by Tukey's post hoc test for multiple comparisons. p values for main effects and interactions are indicated within the figures. The VLDL secretion kinetics in (F, left) was analyzed using simple linear regression. Exact p values are shown for all statistical comparisons. All data are presented as mean ± SEM.

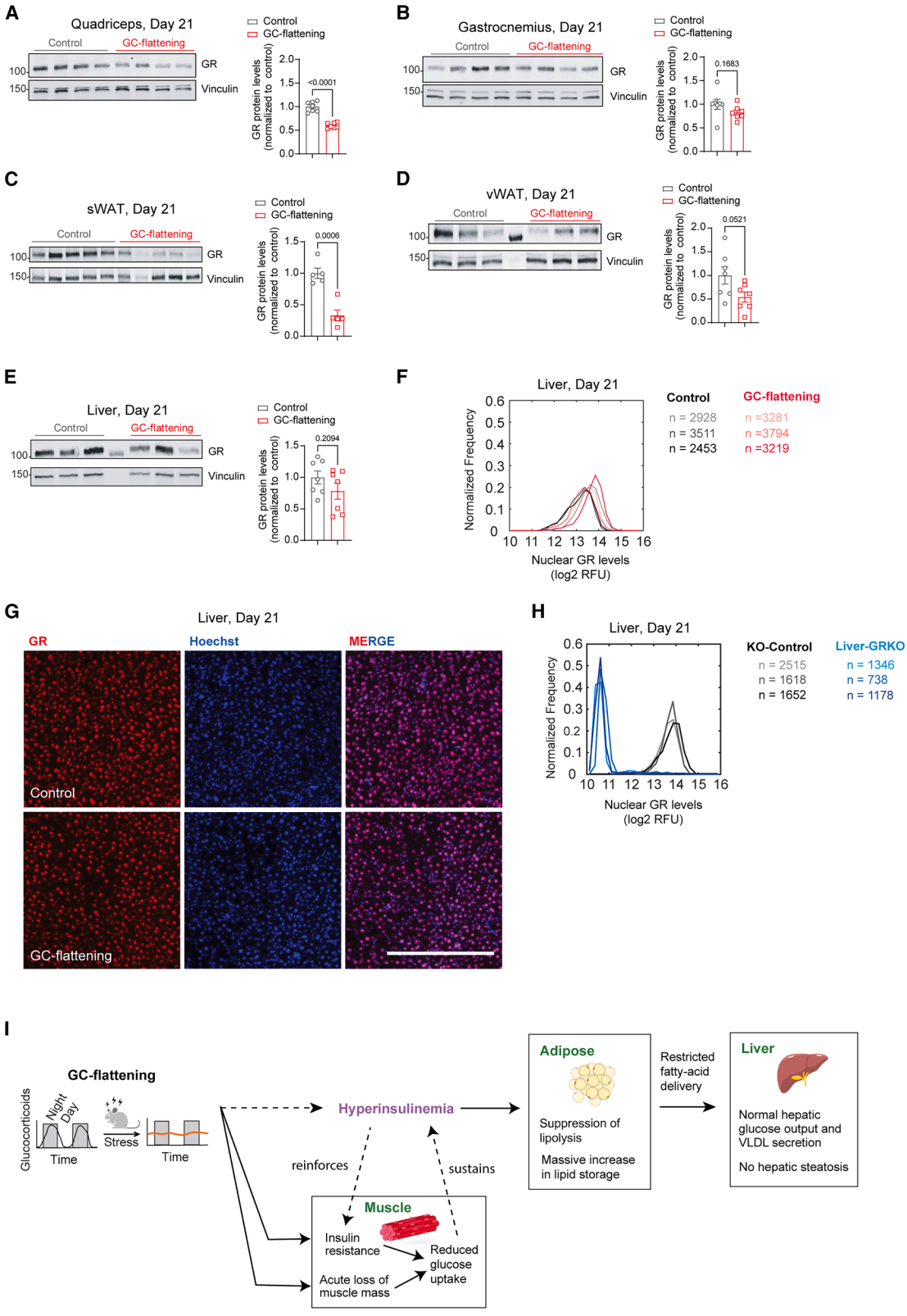

(legend on next page)

control under GC-flattened conditions. The functional outputs of hepatic insulin action remain preserved: insulin suppresses glucose production (Figure 6C), and VLDL secretion and *de novo* lipogenesis are maintained at control levels (Figures 6F and 6G). This suggests that the reduction in insulin receptor abundance is a proportionate counterbalance to the markedly elevated circulating insulin, rather than the selective defect seen in fatty liver, in which insulin fails to restrain glucose output while continuing to drive lipogenesis. The liver likely remains functionally responsive because it is shielded from excess fatty-acid flux from adipose tissue (Figure 5Q). Unlike standard DIO models that exhibit simultaneous impairment in insulin function across muscle, fat, and liver, GC-flattening creates a state where insulin remains functionally effective in the adipose and hepatic compartments. Consequently, this model effectively decouples profound obesity from its typical hepatic pathologies.

Tissue-specific regulation of GR protein abundance

To determine if the divergent outcomes across tissues were a consequence of differential GR regulation, we quantified GR protein abundance following 21 days of GC-flattening. Contrary to a uniform systemic response, we found that GR protein levels were regulated in a highly tissue-specific manner. In skeletal muscle, western blot analysis revealed that GR levels were significantly reduced in the quadriceps (Figure 7A) and exhibited a downward trend in the gastrocnemius (Figure 7B). This downregulation likely represents an adaptive mechanism to limit sustained catabolic signaling, helping to explain why the acute loss of muscle mass observed in this model typically stops after the first week of treatment. These results suggest that the observed stabilization of muscle mass (Figures 2E, 2F, and S2F) is driven by a two-step protective response. First, the reduction in muscle GR abundance decreases the tissue's sensitivity to persistent GC exposure. Second, the rapid induction of sustained hyperinsulinemia (Figure 3C) provides a potent anti-catabolic signal that counteracts GC-induced atrophy.[32] Together, these two hits effectively halt progressive muscle loss despite persistent GC exposure.

White adipose depots similarly appear to adapt in a way that favors lipid retention and limits metabolic overflow. GR protein abundance was significantly reduced in sWAT and showed a downward trend in vWAT (Figures 7C and 7D). Because GC signaling can promote adipose lipolysis, lower GR abundance could reduce the tissue's response to this lipolytic drive. Sustained hyperinsulinemia would reinforce the same effect by strongly suppressing lipolysis. Together, these convergent effects may help maintain suppression of NEFA release and limit fatty-acid delivery to the liver.

Strikingly, GR downregulation was absent in the liver. Western blots showed that hepatic GR protein levels remained stable (Figure 7E), with no significant reduction compared to controls. As a complementary approach to assess hepatic GR abundance, we performed immunofluorescence staining of liver sections from control and GC-flattened mice. Nuclear GR abundance remained unchanged between groups (Figure 7F), consistent with representative images showing robust nuclear localization in both conditions (Figure 7G). To validate antibody specificity, we performed the same analysis in liver-specific GR knockout (L-GRKO) mice. Nuclear GR intensity was markedly reduced in L-GRKO livers compared with KO-controls

Figure 7. Glucocorticoid receptor (GR) abundance is reduced to differing degrees across tissues, and hepatic protection is not explained by loss of receptor from the liver

(A and B) Muscle GR Expression: representative immunoblots and quantification of GR protein abundance in quadriceps (A) and gastrocnemius (B) muscle from control and GC-flattened mice at day 21 of treatment.

(C and D) Adipose GR Expression: representative immunoblots and quantification of GR protein abundance in subcutaneous (sWAT; C) and visceral (vWAT; D) white adipose tissue at day 21.

(E) Hepatic GR Expression: representative immunoblots and quantification of GR protein abundance in the liver at day 21, showing no significant change in GR abundance under GC-flattening.

(F) Nuclear GR Intensity Distributions in Control and GC-flattened Livers: normalized-frequency distributions of single-cell nuclear GR intensity ($\log_2$ RFU) in liver sections from control and GC-flattened mice at day 21. Each curve represents one mouse (n = 3 mice per group). Numbers indicate the total number of nuclei analyzed per mouse across three liver sections.

(G) Hepatic GR Localization: representative liver cryosections from control and GC-flattened mice at day 21 stained with GR antibody (red) and Hoechst (blue). Images correspond to the quantification shown in (F) and are representative of three mice per group. Scale bars, 200 μm.

For (A–G), mice were fasted for 5 h, and tissues were collected 10 min after intraperitoneal insulin injection (5 U/kg body weight), from the same cohort of mice analyzed in Figures 5 and 6.

(H) Nuclear GR Intensity Distributions in L-GRKO Livers: normalized-frequency distributions of single-cell nuclear GR intensity ($\log_2$ RFU) in liver sections from KO-Control and liver-specific GR knockout (L-GRKO) mice. Each curve represents one mouse (n = 3 mice per group). Numbers indicate the total number of nuclei analyzed per mouse across three liver sections. KO-Control and L-GRKO mice were fasted for 5 h and injected intraperitoneally with insulin (0.5 U/kg body weight) 10 min prior to tissue collection. The marked reduction in nuclear GR intensity in L-GRKO livers validates antibody specificity for the immunofluorescence measurements in (F)–(G). See also Figure S7.

(I) Summary Schematic: integrated model of the tissue-specific metabolic response to GC-flattening. Solid arrows indicate relationships supported by data in this study; dashed arrows indicate proposed links that were not tested here. GC-flattening induces acute loss of muscle mass and skeletal muscle insulin resistance, both of which reduce muscle glucose uptake. Hyperinsulinemia may arise through a muscle-independent route and may also be sustained by muscle insulin resistance, and elevated insulin may in turn reinforce that resistance. Insulin acts on adipose tissue that remains insulin-responsive, maintaining suppression of lipolysis and promoting a large increase in lipid storage. This restricts fatty-acid delivery to the liver, allowing hepatic glucose output and VLDL secretion to remain controlled and limiting hepatic steatosis.

Statistical Analysis: vinculin was used as a loading control for all immunoblots in (A)–(E). Each point represents one mouse (n = 5–7 mice per group). Statistical comparisons of protein abundance were performed using two-tailed unpaired t tests. Exact p values are indicated within (A)–(E). The nuclear GR intensity distributions in (F) and (H) are shown descriptively. Each curve represents one mouse and no statistical comparison was performed. All data are presented as mean ± SEM.

(Figure 7H), confirming the specificity of the immunofluorescence signal. Representative images are shown in Figure S7. Because activated GR can undergo ligand-induced turnover, stable receptor abundance is not by itself a measure of GC sensing. We therefore interpret these data as complementary to the hyperinsulinemic-euglycemic clamp results, which provide the primary *in vivo* evidence that insulin-mediated suppression of hepatic glucose output is preserved (Figure 6C). Together, these data show that hepatic protection is not explained by loss of GR from the liver.

An integrated model of tissue-specific metabolic reorganization

Taken together, these tissue-level measurements support a model in which loss of the circadian GC trough reorganizes metabolism through two changes acting in combination (Figure 7I). The first is a reduction in GR abundance in skeletal muscle and adipose tissue, but not in liver. The second is skeletal muscle insulin resistance, which lowers glucose uptake and is accompanied by a several-fold rise in circulating insulin. These two changes converge on the adipose depots: elevated insulin acts on tissue in which pro-lipolytic GC signaling has already been dampened, and the combination produces a sustained anti-lipolytic state that makes adipose tissue a dominant lipid sink.

The consequences for the liver follow from this arrangement. Sequestering lipid in the expanding depots restricts fatty-acid delivery to the liver and prevents the systemic spillover characteristic of DIO, while sustained hyperinsulinemia maintains insulin-mediated suppression of hepatic glucose output (Figure 6C), with VLDL secretion and *de novo* lipogenesis remaining at control levels (Figures 6F and 6G). Hepatic steatosis is therefore limited indirectly, through reduced fatty-acid flux from adipose tissue, rather than through loss of GR from the liver itself.

DISCUSSION

A primary conclusion of this study is that obesity does not manifest as a uniform loss of metabolic control. While it is well established that chronic overnutrition drives the expansion of fat mass, we show that the specific metabolic signature of the obese state is also dictated by the circadian patterning of GC signaling. We show that this hormonal timing determines the tissue-specific distribution of insulin resistance. While traditional DIO results in a global breakdown of insulin action, the loss of GC oscillations, specifically the elimination of the daily trough, reconfigures the system into a state where insulin resistance is partitioned to the skeletal muscle. This specific arrangement allows the organism to maintain a high-capacity lipid sink in the adipose tissue and preserve euglycemia, thereby uncoupling the physical expansion of fat mass from the development of hepatic steatosis.

Within this redistributed pattern of insulin action, skeletal muscle appears particularly sensitive to loss of the daily low-GC period, responding early with catabolic signaling, muscle loss, and insulin resistance. However, this muscle loss is transient rather than progressive. By day 21, GR abundance is reduced in skeletal muscle and adipose tissue, suggesting an adaptive response that may limit continued GC action. At the same time, sustained hyperinsulinemia maintains euglycemia and continues to suppress adipose lipolysis and promote lipid storage. Together, these adaptations help to establish a stable state characterized by increased fat mass and severe muscle insulin resistance, while preserving euglycemia and limiting hepatic lipid accumulation.

Modeling physiological GC rhythm disruption

The GC-flattening paradigm maintains near-normal average physiological GC levels while selectively eliminating circadian rhythmicity. Although mean daily corticosterone was not significantly changed (Figure S1A), total daily exposure was modestly increased (Figure S1B), driven by elevation of the circadian trough. This fits our model, in which sustained catabolic GC signaling arises from loss of the low-GC trough rather than from a change in average hormone levels. This pattern resembles the flattening of GC rhythms observed in humans under chronic stress.[6,14] By removing the daily low-GC recovery periods—while keeping average levels the same—rather than imposing sustained GC excess, our model permits a stable metabolic state in which insulin-dependent control remains functional. In contrast, when GC exposure rises above the physiological range, as with pharmacological dosing or synthetic GCs such as dexamethasone, endocrine feedback can be overwhelmed, driving a loss of metabolic control that progresses to hyperglycemia and hepatic lipid accumulation.

The route of corticosterone delivery was chosen to meet two requirements. First, to flatten the daily rhythm rather than shift or amplify it, we used slow-release subcutaneous pellets, which hold circulating corticosterone at a sustained, non-rhythmic level. Delivery through the drinking water cannot achieve this, because mice drink mainly during the active phase and therefore take in the hormone in a rhythmic pattern.[33] Second, the delivery route matters for the liver, which is central to our conclusion that adiposity can be uncoupled from steatosis. Oral administration would expose the liver to high hormone concentrations through the portal circulation, potentially overstimulating hepatic GRs. Subcutaneous pellets instead release corticosterone systemically, exposing the liver no more than other tissues, so the metabolic phenotype reflects whole-body rhythm disruption rather than localized hepatic steroid overexposure.

Skeletal muscle contributes to sustained hyperinsulinemia

Our results indicate that metabolic health depends on a daily window of hormonal silence, the period of low-GC concentrations. While GC-flattening reduces peak hormone levels, the loss of the GC trough is the primary driver of pathology. First, the resulting phenotype of acute muscle atrophy is a hallmark of excessive GC signaling, not deficiency. Second, this atrophy suggests that rhythm flattening creates persistent signaling activity. While peaks are lower, hormone levels during the rest period remain significantly higher than in rhythmic controls, likely preventing the GR from reaching the low occupancy levels required to fully terminate catabolic gene transcription.

Under GC-flattening conditions, skeletal muscle likely contributes to the hyperinsulinemia. Muscle normally takes up more insulin-stimulated glucose than any other tissue, so resistance in

this tissue increases the amount of insulin required to maintain normal blood glucose. Whether GC signaling in muscle is required for hyperinsulinemia to develop has been tested directly. In muscle-specific GR-knockout mice, deleting GR protected against the hyperinsulinemia, muscle atrophy, and fat gain caused by chronic corticosterone, and blocking insulin production in the same mice prevented the fat gain.[32]

Whether muscle contributes to the initial development of hyperinsulinemia under GC-flattening is harder to judge. The muscle GR-knockout experiments combined two severe manipulations: complete loss of GR from muscle and sustained corticosterone excess.[32] GC-flattening is milder in both respects, since mean GC exposure stays near the physiological range and muscle GR is reduced rather than absent (Figures 7A and 7B). The timing in GC-flattened mice also suggests that muscle may not be the sole site where the hyperinsulinemia begins. Fasting insulin is already several-fold above control by day 3 (Figure 3C), before muscle insulin receptor abundance falls (Figures 5C and 5G). The early rise in insulin may therefore be driven in part by mechanisms independent of muscle insulin resistance, such as direct effects on β-cell insulin secretion or on hepatic insulin clearance, which remain to be tested. Muscle resistance may nonetheless help sustain high insulin once it is established.

Maladaptive versus adaptive signaling and homeostasis

Whether the signaling changes in the GC-flattened model are maladaptive or adaptive depends on the level at which they are viewed. Individually, each of these changes—GR downregulation, persistent muscle catabolic signaling, and muscle insulin resistance—is a hallmark of metabolic dysfunction, yet together they produce a stable, protected state. This apparent paradox follows from the nature of the perturbation. Rhythmic GC signaling is itself a form of metabolic control, exerted through timing, with the daily trough providing a periodic reset. Flattening removes this temporal control, but feedback-based regulation persists: in the GC-flattened state the resulting hyperinsulinemia is potent enough to hold fasting glucose at or below control levels, whereas in HFD the more gradual insulin rise ultimately fails to prevent hyperglycemia (Figures 3A–3F). Stability is thus achieved not through GC rhythms but through adaptive changes in GR abundance and circulating insulin—opposing adjustments that offset one another, each blunting the harm the other would otherwise impose.

Mechanistically, this reorganization is built from two tissue-level changes: a reduction in GR abundance and sustained hyperinsulinemia. By day 21, GR abundance is reduced in both skeletal muscle and adipose tissue, but not in the liver (Figure 7). The consequence of this shared change differs between the two tissues. In adipose tissue, which remains insulin-responsive, reduced GR blunts the response to fat-mobilization signals, so the elevated insulin dominates and drives lipid storage in the expanding depots. In skeletal muscle, the catabolic program remains active, with MuRF1 and Atrogin-1 induced (Figure 2J), even as GR falls (Figures 7A and 7B). Muscle loss is nonetheless transient: lean mass stabilizes and partially recovers within the first 2 weeks (Figures 2E and 2F), most likely driven by the early, several-fold rise in insulin (Figure 3C). Insulin opposes muscle protein breakdown; although the muscle is insulin-resistant, the several-fold excess of circulating insulin is enough to slow proteolysis and keep mass from falling further.

Muscle insulin resistance also has a systemic consequence. What would ordinarily be read as failure—the reduced insulin-receptor abundance, elevated p85, and lower insulin-stimulated pAKT/AKT ratio that mark this resistance (Figure 5)—here becomes part of a protective arrangement: elevated insulin acts on still-responsive adipose tissue to suppress lipolysis, limiting the fatty-acid flux to the liver. The net result is a distinct homeostatic state in which the body tolerates an increase in fat mass to preserve euglycemia and protect the liver under chronic stress.

Distinctions between diet-induced and GC-flattening obesity

In metabolic disease, hyperinsulinemia often serves as an initial compensatory response that maintains normoglycemia during the onset of insulin resistance. The GC-flattening paradigm might therefore appear to be merely an early stage of DIO, before beta-cell failure. However, GC-flattening follows a different path to a different endpoint.

In standard DIO, physiological insulin resistance can develop early while canonical insulin signaling, including AKT phosphorylation, remains largely intact in liver, muscle, and adipose tissue.[31,34] Overnutrition can nevertheless impair insulin's control of adipose lipolysis by disrupting hypothalamic insulin action and increasing sympathetic drive to adipose tissue.[31,34] The resulting increase in fatty-acid delivery to the liver occurs while hepatic insulin signaling remains sufficiently active to drive de novo lipogenesis.[35] Together, increased fatty-acid flux and continued hepatic lipogenesis promote pathological hepatic steatosis in DIO.[31,35]

The GC-flattened model diverges from this trajectory through coordinated recalibration rather than failing compensation. Unlike the largely intact signaling of early DIO, GC-flattening causes a profound downregulation of insulin-signaling machinery specifically in skeletal muscle: by day 21, muscle insulin receptor abundance and insulin-stimulated AKT phosphorylation are significantly reduced (Figure 5). Although this makes muscle a less effective glucose-disposal tissue, the accompanying high, stable insulin levels maintain euglycemia and preserve insulin-mediated suppression of adipose lipolysis, allowing adipose tissue to remain a functional lipid sink. Liver triglycerides are not significantly increased relative to controls and remain far below HFD-fed levels, without increased hepatic lipogenic gene expression or VLDL secretion. Thus, the liver is protected not because obesity is absent or hepatic insulin signaling is entirely unchanged, but likely because fatty-acid delivery from adipose tissue remains constrained and hepatic lipid production is not strongly activated.

These findings distinguish the hepatic phenotype induced by GC-flattening from selective hepatic insulin resistance, in which insulin fails to suppress glucose production yet continues to drive lipogenesis.[36] These two arms of hepatic insulin action are separable: direct hepatocyte insulin signaling is required for lipogenesis but is dispensable for the suppression of glucose production.[35] At the molecular level, GC-flattened livers showed attenuated insulin signaling, with lower insulin receptor

abundance and reduced insulin-stimulated AKT phosphorylation (Figure 6B). However, this did not translate into the functional pattern expected for selective hepatic insulin resistance: insulin-mediated suppression of hepatic glucose output was preserved (Figure 6C), while VLDL secretion and hepatic lipogenic gene expression remained at control levels (Figures 6F and 6G). One interpretation is that preserved adipose insulin action changes the physiological consequences of reduced hepatic insulin signaling. Because adipose tissue remains insulin-responsive in GC-flattened mice, lipolysis is suppressed and fatty-acid delivery to the liver remains low (Figure 5Q). This reduced fatty-acid supply may help preserve suppression of hepatic glucose output despite attenuated proximal insulin signaling in the liver. At the same time, reduced hepatic insulin signaling may limit direct insulin-driven lipogenesis within hepatocytes, consistent with hepatic lipogenic genes remaining at baseline. Thus, GC-flattening does not reproduce the classic selective hepatic insulin-resistance state seen in fatty liver. Instead, the dominant insulin-resistant tissue is skeletal muscle, while adipose lipolysis and hepatic glucose output remain under effective insulin control.

Ultimately, the fundamental difference lies in how glucose and lipid homeostasis are maintained. In DIO, excess nutrient supply and adipose dysfunction progressively overwhelm metabolic control. In GC-flattening, marked hyperinsulinemia coexists with severe muscle insulin resistance, which may help sustain it. Adipose tissue and liver do not share this resistance: the several-fold excess of circulating insulin in GC-flattened mice suppresses lipolysis to the same extent as in controls and holds endogenous glucose production at control levels. Insulin action shifts toward the tissues that remain responsive, preserving euglycemia and diverting lipid into expanding adipose depots instead of the liver. Through this redistribution of insulin action, GC-flattening uncouples increased adiposity from the hepatic pathology typical of DIO.

Endocrine timing and dietary lipids separately control glucose homeostasis and hepatic lipid accumulation

A striking feature of our results is the additive relationship between GC-rhythm flattening and HFD feeding. Both treatments increase adiposity, but they affect glucose homeostasis and hepatic lipid accumulation in distinct ways. With GC-flattening alone, euglycemia is maintained and the liver is largely protected from pathological steatosis. In contrast, HFD feeding promotes hyperglycemia and hepatic lipid accumulation. When GC-flattening and HFD are combined, mice remain euglycemic, but hepatic lipid accumulation is not prevented. This indicates that GC timing and dietary lipid supply make separable contributions to metabolic disease: the temporal pattern of GC signaling strongly influences glucose homeostasis through the tissue-specific organization of insulin action, whereas dietary lipid burden dominates the extent of hepatic lipid accumulation.

The key distinction is that GC-rhythm flattening preserves the systemic insulin signal needed to maintain glucose homeostasis, even during HFD feeding. Sustained hyperinsulinemia appears sufficient to restrain HFD-induced hyperglycemia, consistent with the insulin and glucose time courses shown in Figure 3. However, this same compensatory insulin state does not fully prevent hepatic lipid accumulation when dietary lipid burden is high. Thus, GC-flattening separates glucose control from hepatic lipid accumulation: it preserves euglycemia during HFD feeding, but does not fully protect the liver from HFD-driven lipid accumulation.

Clinical implications

The uncoupling of significant adiposity from pathological hepatic steatosis suggests that BMI may be an insufficient predictor for the development of metabolic dysfunction-associated steatotic liver disease (MASLD). This model provides a biological rationale for why high adiposity does not always result in hepatic steatosis, provided that the adipose-liver axis remains functionally capable of sequestering lipids and preventing the lipotoxic flux characteristic of DIO.

Most current therapeutic strategies focus on improving insulin sensitivity globally. However, our data suggest that under conditions of flattened GC rhythms, muscle insulin resistance may help sustain the hyperinsulinemia required to preserve insulin-mediated suppression of lipolysis in adipose tissue and of glucose output in the liver. In this physiological context, interventions that alter muscle insulin sensitivity could have different systemic consequences depending on whether adipose lipid storage and hepatic insulin-mediated control of glucose output remain intact. This interpretation contrasts with human evidence that skeletal muscle insulin resistance can promote hepatic steatosis. In young, lean, insulin-resistant people, impaired muscle glucose storage diverts ingested carbohydrate to the liver, where hepatic *de novo* lipogenesis and triglyceride synthesis increase, producing atherogenic dyslipidemia and hepatic steatosis.[37] On this basis, restoring muscle insulin sensitivity has been proposed as an early preventive strategy.[37] The different hepatic outcome in our model may depend in part on whether the liver retains the insulin signaling needed to convert excess nutrient flux into fat. Hepatic *de novo* lipogenesis requires direct insulin signaling within hepatocytes.[35] This signaling is intact in lean insulin-resistant subjects, whereas GC-flattened livers show reduced insulin receptor abundance and insulin-stimulated AKT phosphorylation (Figure 6B), with lipogenic gene expression remaining at baseline despite several-fold higher circulating insulin. Nutrient overflow may therefore fuel hepatic lipogenesis when proximal hepatic insulin signaling is intact but not when it is attenuated, although in our model this effect cannot be cleanly separated from the reduced fatty-acid delivery that accompanies it.

Given the formidable obstacles to restoring physiological GC rhythms in a clinical setting, the value of the GC-flattened model lies in its ability to uncover downstream molecular mechanisms that recapitulate the benefits of rhythmic signaling. Identifying pathways that prioritize lipid sequestration, through preservation of a functional adipose-hepatic axis, could inform the development of interventions designed to promote metabolic resilience, even under obesogenic conditions.

Limitations of the study

One limitation of this study is that we applied the GC-flattening protocol for only 8 weeks. It remains possible that more prolonged rhythm disruption—as seen in clinical Cushing's syndrome or certain chronic stress conditions—could

eventually exceed the expansion capacity of the adipose tissue, potentially leading to secondary lipid spillover and late-stage hepatic steatosis.

A second limitation is the transient rise in circulating GCs that occurs during the first 24 h after corticosterone-pellet implantation. Thus, we cannot fully exclude the possibility that this initial GC surge contributes to the early metabolic responses. This elevation, which does not occur in placebo controls, likely reflects a physiological resetting of the hypothalamic-pituitary-adrenal (HPA) axis in response to elevated trough-phase GCs. Because this brief overshoot arises from normal HPA-axis feedback rather than from the delivery method itself, it would likely occur with any approach that imposes constant GC exposure. The surge is short relative to the 8-week intervention and resembles the acute GC elevations seen during natural stress responses, so it is unlikely to drive the long-term metabolic phenotypes observed here.

A third limitation is that this study used only male mice. Sex differences in GC signaling, adipose distribution, and insulin sensitivity are well documented, so whether the muscle-selective insulin resistance and hepatic protection described here generalize to females remains to be determined.

RESOURCE AVAILABILITY

Lead contact

Further information and requests for resources and reagents should be directed to and will be fulfilled by the lead contact, Mary N. Teruel (mnt4002@med.cornell.edu).

Materials availability

This study did not generate any new reagents.

Data and code availability

Source data for all graphs used in the figures are provided in Data S1. Original uncropped western blots are provided in Data S2. This paper does not report original code. Any additional information required to reanalyze the data reported in this paper is available from the lead contact upon request.

ACKNOWLEDGMENTS

This work was supported by NIH R01DK131432 (M.N.T.), startup funds from the Drukier Institute and Weill Cornell Medicine (M.N.T.), NIH T32DK131957 fellowship (A.A.), American Diabetes Association fellowship 1–26-PDF-1121 (L.P.J.S.), NIH DK132427 and CA258697 (C.E.E., J.G., and M.D.G.), and NIH T32GM152349 (I.N.). We thank Tobias Meyer, Laura Alonso, Baran Ersoy, Shannon Reilly, all members of the Teruel lab and Meyer lab (Weill Cornell Medicine), and Fredric Kraemer (Stanford) for helpful discussions. Hyperinsulinemic-euglycemic clamps were performed by the Vanderbilt Mouse Metabolic Phenotyping Center (DK020593, DK135073). The Vanderbilt Hormone Assay and Analytical Core performed insulin and NEFA analyses (DK020593).

AUTHOR CONTRIBUTIONS

A.A., S.S., and M.N.T. designed the study; A.A., S.S., A.N., L.P.J.S., J.W., J.L., L.Y., A.S.A., L.L., E.K., A.U., C.E.E., K.R.F., I.N., J.G., E.D.K., R.J., and R.P. performed experiments; A.A., S.S., A.N., L.P.J.S., J.W., L.Y., A.S.A., L.L., E.K., A.U., K.R.F., E.D.K., R.J., R.P., T.T., and M.N.T. collected and analyzed data; and T.T., M.D.G., T.E.M., and M.N.T. provided technical support and conceptual advice; M.N.T. supervised the study and acquired funding; A.A., S.S., and M.N.T. wrote the manuscript with input from all authors.

DECLARATION OF INTERESTS

The authors declare no competing interests.

STAR★METHODS

Detailed methods are provided in the online version of this paper and include the following:

- KEY RESOURCES TABLE
- EXPERIMENTAL MODEL AND STUDY PARTICIPANT DETAILS
- METHOD DETAILS
  - Fasting conditions and sample collection
  - Fasting glucose and insulin measurements
  - Tolerance tests
  - Corticosterone administration in mice
  - Measurement of corticosterone in blood plasma
  - Liver Oil Red O staining
  - Liver H&E histology
  - Liver glucocorticoid receptor immunofluorescence
  - Measurement of liver triglycerides
  - Measurement of plasma triglycerides and hepatic VLDL secretion rates
  - Measurement of plasma non-esterified fatty acids (NEFAs)
  - Adipose tissue histology and analysis
  - Necropsies
  - Amino acid analysis
  - Skeletal muscle tissue histology and analysis
  - Body composition
  - Hyperinsulinemic–euglycemic clamp
  - RNA isolation and quantitative RT-PCR analysis
  - Western Blot analysis
- QUANTIFICATION AND STATISTICAL ANALYSIS

SUPPLEMENTAL INFORMATION

Supplemental information can be found online at https://doi.org/10.1016/j.celrep.2026.117926.

Received: March 24, 2025
Revised: June 28, 2026
Accepted: August 13, 2026

REFERENCES

1. Blüher, M. (2019). Obesity: global epidemiology and pathogenesis. Nat. Rev. Endocrinol. *15*, 288–298. https://doi.org/10.1038/s41574-019-0176-8.
2. Broussard, J.L., and Van Cauter, E. (2016). Disturbances of sleep and circadian rhythms: novel risk factors for obesity. Curr. Opin. Endocrinol. Diabetes Obes. *23*, 353–359. https://doi.org/10.1097/MED.0000000000000276.
3. Chaput, J.-P., McHill, A.W., Cox, R.C., Broussard, J.L., Dutil, C., Da Costa, B.G.G., Sampasa-Kanyinga, H., and Wright, K.P. (2023). The role of insufficient sleep and circadian misalignment in obesity. Nat. Rev. Endocrinol. *19*, 82–97. https://doi.org/10.1038/s41574-022-00747-7.
4. Vegiopoulos, A., and Herzig, S. (2007). Glucocorticoids, metabolism and metabolic diseases. Mol. Cell. Endocrinol. *275*, 43–61. https://doi.org/10.1016/j.mce.2007.05.015.
5. Leproult, R., and Van Cauter, E. (2010). Role of Sleep and Sleep Loss in Hormonal Release and Metabolism. In Endocrine Development, S. Loche, M. Cappa, L. Ghizzoni, M. Maghnie, and M.O. Savage, eds. (S. Karger AG), pp. 11–21. https://doi.org/10.1159/000262524.
6. Dallman, M.F., Akana, S.F., Bhatnagar, S., Bell, M.E., and Strack, A.M. (2000). Bottomed out: metabolic significance of the circadian trough in glucocorticoid concentrations. Int. J. Obes. Relat. Metab. Disord. *24*, S40–S46. https://doi.org/10.1038/sj.ijo.0801276.

7. Weitzman, E.D., Fukushima, D., Nogeire, C., Roffwarg, H., Gallagher, T.F., and Hellman, L. (1971). Twenty-four Hour Pattern of the Episodic Secretion of Cortisol in Normal Subjects. J. Clin. Endocrinol. Metab. *33*, 14–22. https://doi.org/10.1210/jcem-33-1-14.

8. Fekedulegn, D., Burchfiel, C.M., Violanti, J.M., Hartley, T.A., Charles, L.E., Andrew, M.E., and Miller, D.B. (2012). Associations of Long-term Shift Work with Waking Salivary Cortisol Concentration and Patterns among Police Officers. Ind. Health *50*, 476–486. https://doi.org/10.2486/indhealth.2012-0043.

9. Leproult, R., Copinschi, G., Buxton, O., and Van Cauter, E. (1997). Sleep Loss Results in an Elevation of Cortisol Levels the Next Evening. Sleep *20*, 865–870. https://doi.org/10.1093/sleep/20.10.865.

10. Bahrami-Nejad, Z., Zhao, M.L., Tholen, S., Hunerdosse, D., Tkach, K.E., van Schie, S., Chung, M., and Teruel, M.N. (2018). A Transcriptional Circuit Filters Oscillating Circadian Hormonal Inputs to Regulate Fat Cell Differentiation. Cell Metab. *27*, 854–868.e8. https://doi.org/10.1016/j.cmet.2018.03.012.

11. Tholen, S., Patel, R., Agas, A., Kovary, K.M., Rabiee, A., Nicholls, H.T., Bielczyk-Maczyńska, E., Yang, W., Kraemer, F.B., and Teruel, M.N. (2022). Flattening of circadian glucocorticoid oscillations drives acute hyperinsulinemia and adipocyte hypertrophy. Cell Rep. *39*, 111018. https://doi.org/10.1016/j.celrep.2022.111018.

12. Meijer, O.C., Kooijman, S., Kroon, J., and Winter, E.M. (2023). The importance of the circadian trough in glucocorticoid signaling: a variation on B-flat. Stress *26*, 2275210. https://doi.org/10.1080/10253890.2023.2275210.

13. Al-Safi, Z.A., Polotsky, A., Chosich, J., Roth, L., Allshouse, A.A., Bradford, A.P., and Santoro, N. (2018). Evidence for disruption of normal circadian cortisol rhythm in women with obesity. Gynecol. Endocrinol. *34*, 336–340. https://doi.org/10.1080/09513590.2017.1393511.

14. Rosmond, R., Dallman, M.F., and Björntorp, P. (1998). Stress-Related Cortisol Secretion in Men: Relationships with Abdominal Obesity and Endocrine, Metabolic and Hemodynamic Abnormalities. J. Clin. Endocrinol. Metab. *83*, 1853–1859. https://doi.org/10.1210/jcem.83.6.4843.

15. Imamura, F., Micha, R., Khatibzadeh, S., Fahimi, S., Shi, P., Powles, J., and Mozaffarian, D.; Global Burden of Diseases Nutrition and Chronic Diseases Expert Group NutriCoDE (2015). Dietary quality among men and women in 187 countries in 1990 and 2010: a systematic assessment. Lancet. Glob. Health *3*, e132–e142. https://doi.org/10.1016/S2214-109X(14)70381-X.

16. Micha, R., Khatibzadeh, S., Shi, P., Fahimi, S., Lim, S., Andrews, K.G., Engell, R.E., Powles, J., Ezzati, M., and Mozaffarian, D.; Global Burden of Diseases Nutrition and Chronic Diseases Expert Group NutriCoDE (2014). Global, regional, and national consumption levels of dietary fats and oils in 1990 and 2010: a systematic analysis including 266 country-specific nutrition surveys. BMJ *348*, g2272. https://doi.org/10.1136/bmj.g2272.

17. Monteiro, C.A., Moubarac, J.-C., Cannon, G., Ng, S.W., and Popkin, B. (2013). Ultra-processed products are becoming dominant in the global food system. Obes. Rev. *14*, 21–28. https://doi.org/10.1111/obr.12107.

18. Popkin, B.M., Adair, L.S., and Ng, S.W. (2012). Global nutrition transition and the pandemic of obesity in developing countries. Nutr. Rev. *70*, 3–21. https://doi.org/10.1111/j.1753-4887.2011.00456.x.

19. Sapolsky, R.M., Krey, L.C., and McEwen, B.S. (1986). The Neuroendocrinology of Stress and Aging: The Glucocorticoid Cascade Hypothesis. Endocr. Rev. *7*, 284–301. https://doi.org/10.1210/edrv-7-3-284.

20. Hodes, G.E., Brookshire, B.R., Hill-Smith, T.E., Teegarden, S.L., Berton, O., and Lucki, I. (2012). Strain differences in the effects of chronic corticosterone exposure in the hippocampus. Neuroscience *222*, 269–280. https://doi.org/10.1016/j.neuroscience.2012.06.017.

21. Rosen, E.D., and Spiegelman, B.M. (2014). What We Talk About When We Talk About Fat. Cell *156*, 20–44. https://doi.org/10.1016/j.cell.2013.12.012.

22. Spalding, K.L., Bernard, S., Näslund, E., Salehpour, M., Possnert, G., Appelsved, L., Fu, K.-Y., Alkass, K., Druid, H., Thorell, A., et al. (2017). Impact of fat mass and distribution on lipid turnover in human adipose tissue. Nat. Commun. *8*, 15253. https://doi.org/10.1038/ncomms15253.

23. Schakman, O., Gilson, H., and Thissen, J.P. (2008). Mechanisms of glucocorticoid-induced myopathy. J. Endocrinol. *197*, 1–10. https://doi.org/10.1677/JOE-07-0606.

24. Lei, L., Li, Y., Li, M., Xin, H., Tian, X., Zhang, Y., Shi, W., and Cong, B. (2024). Pathological changes in the spleen of mice subjected to different time courses of restraint stress. Sci. Rep. *14*, 13543. https://doi.org/10.1038/s41598-024-64475-w.

25. Kuo, T., Lew, M.J., Mayba, O., Harris, C.A., Speed, T.P., and Wang, J.-C. (2012). Genome-wide analysis of glucocorticoid receptor-binding sites in myotubes identifies gene networks modulating insulin signaling. Proc. Natl. Acad. Sci. USA *109*, 11160–11165. https://doi.org/10.1073/pnas.1111334109.

26. Kahn, S.E., Hull, R.L., and Utzschneider, K.M. (2006). Mechanisms linking obesity to insulin resistance and type 2 diabetes. Nature *444*, 840–846. https://doi.org/10.1038/nature05482.

27. Weir, G.C., and Bonner-Weir, S. (2004). Five Stages of Evolving β-Cell Dysfunction During Progression to Diabetes. Diabetes *53*, S16–S21. https://doi.org/10.2337/diabetes.53.suppl_3.S16.

28. Ayala, J.E., Bracy, D.P., McGuinness, O.P., and Wasserman, D.H. (2006). Considerations in the Design of Hyperinsulinemic–euglycemic Clamps in the Conscious Mouse. Diabetes *55*, 390–397. https://doi.org/10.2337/diabetes.55.02.06.db05-0686.

29. Alquier, T., and Poitout, V. (2018). Considerations and guidelines for mouse metabolic phenotyping in diabetes research. Diabetologia *61*, 526–538. https://doi.org/10.1007/s00125-017-4495-9.

30. Barbour, L.A., Rahman, S.M., Gurevich, I., Leitner, J.W., Fischer, S.J., Roper, M.D., Knotts, T.A., Vo, Y., McCurdy, C.E., Yakar, S., et al. (2005). Increased P85α Is a Potent Negative Regulator of Skeletal Muscle Insulin Signaling and Induces in Vivo Insulin Resistance Associated with Growth Hormone Excess. J. Biol. Chem. *280*, 37489–37494. https://doi.org/10.1074/jbc.M506967200.

31. Sakamoto, K., Butera, M.A., Zhou, C., Maurizi, G., Chen, B., Ling, L., Shawkat, A., Patlolla, L., Thakker, K., Calle, V., et al. (2025). Overnutrition causes insulin resistance and metabolic disorder through increased sympathetic nervous system activity. Cell Metab. *37*, 121–137.e6. https://doi.org/10.1016/j.cmet.2024.09.012.

32. Yamazaki, H., Uehara, M., Yoshikawa, N., Kuribara-Souta, A., Yamamoto, M., Hirakawa, Y., Kabe, Y., Suematsu, M., and Tanaka, H. (2023). The crucial role of muscle glucocorticoid signaling in accelerating obesity and glucose intolerance via hyperinsulinemia. JCI Insight *8*, e162382. https://doi.org/10.1172/jci.insight.162382.

33. Gasparini, S.J., Weber, M.-C., Henneicke, H., Kim, S., Zhou, H., and Seibel, M.J. (2016). Continuous corticosterone delivery via the drinking water or pellet implantation: A comparative study in mice. Steroids *116*, 76–82. https://doi.org/10.1016/j.steroids.2016.10.008.

34. Scherer, T., Lindtner, C., Zielinski, E., O'Hare, J., Filatova, N., and Buettner, C. (2012). Short Term Voluntary Overfeeding Disrupts Brain Insulin Control of Adipose Tissue Lipolysis. J. Biol. Chem. *287*, 33061–33069. https://doi.org/10.1074/jbc.M111.307348.

35. Titchenell, P.M., Quinn, W.J., Lu, M., Chu, Q., Lu, W., Li, C., Chen, H., Monks, B.R., Chen, J., Rabinowitz, J.D., and Birnbaum, M.J. (2016). Direct Hepatocyte Insulin Signaling Is Required for Lipogenesis but Is Dispensable for the Suppression of Glucose Production. Cell Metab. *23*, 1154–1166. https://doi.org/10.1016/j.cmet.2016.04.022.

36. Brown, M.S., and Goldstein, J.L. (2008). Selective versus Total Insulin Resistance: A Pathogenic Paradox. Cell Metab. *7*, 95–96. https://doi.org/10.1016/j.cmet.2007.12.009.

37. Petersen, K.F., Dufour, S., Savage, D.B., Bilz, S., Solomon, G., Yonemitsu, S., Cline, G.W., Befroy, D., Zemany, L., Kahn, B.B., et al. (2007). The role of

skeletal muscle insulin resistance in the pathogenesis of the metabolic syndrome. Proc. Natl. Acad. Sci. USA *104*, 12587–12594. https://doi.org/10.1073/pnas.0705408104.

38. Bankhead, P., Loughrey, M.B., Fernández, J.A., Dombrowski, Y., McArt, D.G., Dunne, P.D., McQuaid, S., Gray, R.T., Murray, L.J., Coleman, H.G., et al. (2017). QuPath: Open source software for digital pathology image analysis. Sci. Rep. *7*, 16878. https://doi.org/10.1038/s41598-017-17204-5.
39. Stringer, C., Wang, T., Michaelos, M., and Pachitariu, M. (2021). Cellpose: a generalist algorithm for cellular segmentation. Nat. Methods *18*, 100–106. https://doi.org/10.1038/s41592-020-01018-x.
40. Folch, J., Lees, M., and Stanley, G.H.S. (1957). A SIMPLE METHOD FOR THE ISOLATION AND PURIFICATION OF TOTAL LIPIDES FROM ANIMAL TISSUES. J. Biol. Chem. *226*, 497–509. https://doi.org/10.1016/S0021-9258(18)64849-5.
41. Steensels, S., Qiao, J., Zhang, Y., Maner-Smith, K.M., Kika, N., Holman, C.D., Corey, K.E., Bracken, W.C., Ortlund, E.A., and Ersoy, B.A. (2020). Acyl-Coenzyme A Thioesterase 9 Traffics Mitochondrial Short-Chain Fatty Acids Toward De Novo Lipogenesis and Glucose Production in the Liver. Hepatology *72*, 857–872. https://doi.org/10.1002/hep.31409.
42. Goncalves, M.D., Hwang, S.-K., Pauli, C., Murphy, C.J., Cheng, Z., Hopkins, B.D., Wu, D., Loughran, R.M., Emerling, B.M., Zhang, G., et al. (2018). Fenofibrate prevents skeletal muscle loss in mice with lung cancer. Proc. Natl. Acad. Sci. USA *115*, E743–E752. https://doi.org/10.1073/pnas.1714703115.
43. TeSlaa, T., Bartman, C.R., Jankowski, C.S.R., Zhang, Z., Xu, X., Xing, X., Wang, L., Lu, W., Hui, S., and Rabinowitz, J.D. (2021). The Source of Glycolytic Intermediates in Mammalian Tissues. Cell Metab. *33*, 367–378.e5. https://doi.org/10.1016/j.cmet.2020.12.020.
44. Hui, S., Ghergurovich, J.M., Morscher, R.J., Jang, C., Teng, X., Lu, W., Esparza, L.A., Reya, T., Zhan, L., Guo, J.Y., et al. (2017). Glucose feeds the TCA cycle via circulating lactate. Nature *551*, 115–118. https://doi.org/10.1038/nature24057.
45. Battey, E., Dos Santos, M., Biswas, D., Maire, P., and Sakamoto, K. (2024). Protocol for muscle fiber type and cross-sectional area analysis in cryosections of whole lower mouse hindlimbs. STAR Protoc. *5*, 103424. https://doi.org/10.1016/j.xpro.2024.103424.
46. Berglund, E.D., Li, C.Y., Poffenberger, G., Ayala, J.E., Fueger, P.T., Willis, S.E., Jewell, M.M., Powers, A.C., and Wasserman, D.H. (2008). Glucose Metabolism In Vivo in Four Commonly Used Inbred Mouse Strains. Diabetes *57*, 1790–1799. https://doi.org/10.2337/db07-1615.
47. Finegood, D.T., Bergman, R.N., and Vranic, M. (1987). Estimation of Endogenous Glucose Production During Hyperinsulinemic–euglycemic Glucose Clamps. Diabetes *36*, 914–924. https://doi.org/10.2337/diab.36.8.914.
48. Steele, R., Wall, J.S., De Bodo, R.C., and Altszuler, N. (1956). Measurement of Size and Turnover Rate of Body Glucose Pool by the Isotope Dilution Method. Am. J. Physiol. *187*, 15–24. https://doi.org/10.1152/ajplegacy.1956.187.1.15.
49. Kraegen, E.W., James, D.E., Jenkins, A.B., and Chisholm, D.J. (1985). Dose-response curves for in vivo insulin sensitivity in individual tissues in rats. Am. J. Physiol. *248*, E353–E362. https://doi.org/10.1152/ajpendo.1985.248.3.E353.

STAR★METHODS

KEY RESOURCES TABLE

REAGENT or RESOURCE	SOURCE	IDENTIFIER
Antibodies		
Gapdh (D16H11) XP® Rabbit mAb	Cell Signaling Technology	Cat#5174, RRID:AB_10622025
Akt Antibody	Cell Signaling Technology	Cat#9272, RRID: AB_329827
phospho-Akt (Ser473) Antibody	Cell Signaling Technology	Cat#9271, RRID:AB_329825
Insulin Receptor β (E9L5V) XP® Rabbit mAb	Cell Signaling Technology	Cat#23413, RRID:AB_2924796
Vinculin	Thermo Fisher Scientific	Cat#14–9777-80, RRID:AB_2573027
p85	Cell Signaling	Cat#4257, RRID:AB_659889
Glucocorticoid receptor	Cell Signaling	Cat#12041, RRID:AB_2631286
Goat anti-rabbit IgG (H + L), Alexa Fluor 647	Invitrogen/Thermo Fisher Scientific	Cat#A-21245, RRID:AB_2535813
MyHC type I (mouse IgG2b monoclonal)	DSHB	Cat#BA-F8, RRID:AB_10572253
MyHC type IIA (mouse IgG1 monoclonal)	DSHB	Cat#SC-71, RRID:AB_2147165
MyHC type IIB (mouse IgM monoclonal)	DSHB	Cat#BF-F3, RRID:AB_2266724
Laminin (rat IgG1 monoclonal)	Sigma-Aldrich	Cat#L0663, RRID:AB_477153
Goat anti- mouse IgG2b (Alexa Fluor 647)	Thermo Fisher Scientific	Cat#A21242, RRID:AB_2535811
Goat anti-mouse IgG1 (Alexa Fluor 488)	Thermo Fisher Scientific	Cat#A21121, RRID:AB_2535764
Goat anti-mouse IgM (Alexa Fluor 568)	Thermo Fisher Scientific	Cat#A21043, RRID:AB_2535712
Goat anti-rat IgG1 (Alexa Fluor Plus 405)	Thermo Fisher Scientific	Cat#A48261, RRID:AB_2890550
Goat anti- rabbit (Alexa Fluor 680)	Thermo Fisher Scientific	Cat#A21109, RRID:AB_2535758
IRDye CW Goat anti-mouse 800CW	LICORbio	Cat#926–32210, RRID:AB_621842
Anti-rabbit IgG, HRP-linked	Cell Signaling Technology	Cat#7074, RRID:AB_2099233
Bacterial and virus strains		
AAV8-TBG-iCre (adeno-associated virus serotype 8 expressing codon-improved Cre recombinase under the hepatocyte-specific thyroxine-binding globulin promoter; used to generate Liver-GRKO mice)	Vector Biolabs	Cat#VB1724
AAV8-TBG-LacZ (control adeno-associated virus serotype 8 expressing LacZ under the thyroxine-binding globulin promoter; used to generate KO-Control mice)	Vector Biolabs	Cat#70003-S
Chemicals, peptides, and recombinant proteins		
Corticosterone pellets (15mg, 60-day release)	Innovative Research of America	Cat#SG-111
Placebo pellets (15mg, 60-day release)	Innovative Research of America	Cat#SC-111
Corticosterone pellets (5mg, 21-day release)	Innovative Research of America	Cat#G-111
Placebo pellets (5mg, 21-day release)	Innovative Research of America	Cat#C-111
Glucose	Sigma-Aldrich	Cat#G8270
Humulin® R (U-100)	Lilly	N/A
60% High-Fat-Diet	Research Diets	Cat#D12492
Oil Red O	Sigma-Aldrich	Cat#O-0625
Tyloxapol	Sigma-Aldrich	Cat#T8761
TRIzol	Thermo Fisher Scientific	Cat#488201
SuperSignal West Pico PLUS Chemiluminescent Substrate	Thermo Fisher Scientific	Cat#34580
Paraformaldehyde	Electron Microscopy Sciences	Cat#15710-S
Hoechst 33342	Invitrogen/Thermo Fisher Scientific	Cat#62249
Fluoromount-G	Electron Microscopy Sciences	Cat#17984–25

(*Continued on next page*)

Continued		
REAGENT or RESOURCE	SOURCE	IDENTIFIER
VectaMount aqueous mounting medium	Vector Laboratories	Cat#H-5501
Normal goat serum	Jackson ImmunoResearch	Cat #005–000-121
Critical commercial assays		
Corticosterone Multi-Format ELISA Kit	Arbor Assays	Cat#K014-H1
Ultra-Sensitive Mouse Insulin ELISA Kit	Crystal Chem	Cat#90080
L-Type Triglyceride M Enzyme Color A	Fujifilm Wako	Cat#994–02891
L-Type Triglyceride M Buffer Solution A	Fujifilm Wako	Cat#992–02892
L-Type Triglyceride M Enzyme Color B	Fujifilm Wako	Cat#990–02991
L-Type Triglyceride M Buffer Solution B	Fujifilm Wako	Cat#998–02992
Multi-Calibrator Lipid	Fujifilm Wako	Cat#464–01601
HR Series NEFA-HR(2) Color Reagent A	Fujifilm Wako	Cat#999–34691
HR Series NEFA-HR(2) Solvent A	Fujifilm Wako	Cat#995–34791
HR Series NEFA-HR(2) Color Reagent B	Fujifilm Wako	Cat#991–34891
HR Series NEFA-HR(2) Solvent B	Fujifilm Wako	Cat#993–35191
NEFA Standard Solution	Fujifilm Wako	Cat#276–76491
Diathrive Blood Glucose Test Strips	Diathrive Health	N/A
RNeasy Mini Kit	Qiagen	Cat#74106
qScript™ cDNA Synthesis Kit	Quantabio	Cat#95047
PowerTrack™ SYBR Green Master Mix	Applied Biosystems	Cat# A46109
BlasTaq™ 2X qPCR MasterMix	ABM	Cat #G891
Experimental models: Organisms/strains		
Mice: C57BL/6J	Jackson Labs	Cat#000664; RRID (IMSR_JAX:000664)
Mice: Nr3c1$^{fl/fl}$ (GR$^{fl/fl}$; B6.Cg-Nr3c1$^{tm1.1Jda}$/J); injected with AAV8-TBG-iCre to generate hepatocyte-specific GR knockout (Liver-GRKO) mice, or with AAV8-TBG-LacZ to generate KO-Control mice	Jackson Labs	Cat#021021; RRID (IMSR_JAX:021021)
Oligonucleotides		
See Table S1	This paper	N/A
Software and algorithms		
ImageJ	NIH	https://imagej.nih.gov/ij/download.html
Fiji macro toolset MRI Adipocytes Tools	Montpellier Ressources Imagerie	https://github.com/MontpellierRessourcesImagerie/imagej_macros_and_scripts
ImageJ plugin Watershed Algorithm	ImageJ	https://imagej.net/ij/plugins/watershed.html
GraphPad Prism 10	GraphPad Software	https://www.graphpad.com/scientific-software/prism/
QuPath (v0.6.0)	Bankhead[38]	https://qupath.github.io/
QuPath Cellpose extension	Stringer[39]	https://github.com/BIOP/qupath-extension-cellpose

EXPERIMENTAL MODEL AND STUDY PARTICIPANT DETAILS

Seven-week-old C57BL/6J male mice (Jackson Laboratory, cat. 000664) were housed at the Weill Cornell Medicine animal facility. After a 7-day acclimatization, mice were maintained on a 12h light/dark cycle (lights on at 6:00 a.m.) with free access to drinking water and standard chow diet (PicoLab Rodent Diet 20, 5053; Lab Diets, St. Louis, MO), except during fasting periods. For diet-induced obesity studies, mice were fed a High-Fat Diet (HFD; 60% kcal from fat; D12492; Research Diets, New Brunswick, NJ) *ad libitum*. Individual mice were identified by ear tags, and researchers remained blinded to treatment groups. Experimental and control groups were matched for baseline body weight using a block randomization method to ensure equal average starting weights. To minimize cage-to-cage variations, experimental and control mice were mixed within the same cages.

To generate hepatocyte-specific glucocorticoid receptor knockout (Liver-GRKO) mice, we used *Nr3c1*$^{fl/fl}$ mice (hereafter GR$^{fl/fl}$; B6.Cg-*Nr3c1*$^{tm1.1Jda}$/J; Jackson Laboratory, stock #021021), which carry *loxP* sites flanking exon 3 of *Nr3c1* and are maintained on a C57BL/6J background. Male GR$^{fl/fl}$ mice received a single retro-orbital injection of 100 μL of a serotype 8 adeno-associated virus expressing codon-improved Cre recombinase under the control of the hepatocyte-specific thyroxine-binding globulin (TBG) promoter (AAV8-TBG-iCre; Vector Biolabs, cat. #VB1724; 2×10^{11} genome copies diluted in sterile PBS). Control (KO-Control) mice were GR$^{fl/fl}$ littermates that received an equivalent dose of AAV8-TBG-LacZ (Vector Biolabs, cat. #70003-S). Housing, diet, randomization, and blinding were as described above for C57BL/6J mice. Pellet implantation and all subsequent experiments were started seven days after AAV8 injection.

All animal procedures were approved by the Institutional Animal Care and Use Committee (IACUC) of Weill Cornell Medical College (Protocol #2020-0001), except for the hyperinsulinemic–euglycemic clamp studies, which were approved by the IACUC of Vanderbilt University (Protocol #M1500013-03). All experiments were performed in accordance with the NIH Guide for the Care and Use of Laboratory Animals and applicable institutional and federal regulations.

METHOD DETAILS

Fasting conditions and sample collection

Throughout this manuscript, ''fasted'' mice refer to animals placed in clean cages, ensuring no access to food, food dust, or feces in the bedding, for 5 h during the light cycle (typically 9:00 AM-2:00 PM). Water was freely available during fasting. Unless otherwise noted, mice were fasted prior to blood and tissue collection. Blood was collected by tail snip or cardiac puncture into ethylenediaminetetraacetic acid (EDTA) coated tubes, centrifuged (6,000 x g for 20 min at 4°C), and the plasma supernatant was stored at −20°C. All dissections were performed between 2:00 p.m. and 6:00 p.m., alternating between corticosterone-treated and control mice. Harvested tissue samples were either fixed in buffered zinc formalin fixative (Cancer Diagnostics Inc., 171) for paraffin embedding, or snap-frozen in liquid nitrogen and stored at −80°C.

Fasting glucose and insulin measurements

For fasting glucose and insulin measurements, mice were fasted for 5 h as described above, with sample collection performed between 2:00 PM-6:00 PM. Blood was drawn via tail snip, and glucose levels were measured with a glucometer (Diathrive, Salt Lake City, Utah). An additional 30 μL of blood for insulin measurements was collected into EDTA-coated tubes for plasma separation. For subsequent weekly blood collections, samples were taken by removing the scab from the previous draw site. Plasma insulin concentration was determined using the Ultra-Sensitive Mouse Insulin ELISA Kit (Cat. 90080, CrystalChem, Illinois, USA) according to the manufacturer's instructions.

Tolerance tests

Prior to glucose tolerance test (GTT) and insulin tolerance test (ITT) procedures, mice were fasted for 5 h starting at 9:00 a.m., as described in ''Fasting Conditions and Sample Collection.'' For GTT, mice received an intraperitoneal injection of 2 g glucose (Sigma G8270)/kg body weight. For ITT, mice were injected intraperitoneally with 0.75 units/kg body weight of human insulin (Humulin R (U-100), Eli Lilly). Blood samples for glucose level measurements were collected immediately before injection, and at 15, 30, 45, 60, and 120 min post-injection. Samples were analyzed as described above.

Corticosterone administration in mice

To flatten circadian glucocorticoid (GC) oscillations, mice were implanted subcutaneously with pellets that released corticosterone for either 21 days or 60 days (21-day release, 5 mg, Catalog number G-111; 60-day release, 15 mg total, Catalog number SG-111; Innovative Research of America, Sarasota, FL, USA). Placebo pellets (Catalog number C-111 or SC-111) were implanted as control. Prior to pellet implantation, mice were anesthetized via continuous inhalation of isoflurane. Once anesthetized, an incision equal in diameter to that of the pellet was made on the lateral side of the neck, and the pellet was inserted 2 cm from the incision site using forceps or a trocar. At day of implantation, mice weighed an average of 24.1 ± 1.2 g, which resulted in a daily dose of 10 mg/kg/day.

Measurement of corticosterone in blood plasma

Blood was taken at multiple time points (8:00, 11:00, 14:00, 17:00, 18:30, 20:00, and 23:00) over a 15 h time period. At the first time point, blood was taken by nicking the tail vein. Blood samples collected at subsequent time points were taken by removing the crust formed after first blood withdrawal. The corticosterone concentration in blood plasma was determined using the Enzyme Immunoassay kit (K014-H1, Arbor Assays, Michigan, USA) following the manufacturer's instructions.

Liver Oil Red O staining

Liver samples from the largest lobe were snap-frozen in liquid nitrogen and stored at −80°C. Frozen livers were sectioned at 10 μm on a Leica cryostat, mounted on positively charged glass slides, and stored at −20°C until staining. Working Oil Red O solution was prepared by saturating Oil Red O (Sigma, #O-0625) in 99% isopropanol (Fisher Scientific, #A451-4), diluting to 60% with distilled water, and filtering through Whatman paper (Grainger, #1002-185) before use. Slides were dried at room temperature for 30 min, dipped

once in 60% isopropanol, stained in working solution for 5 min, then dipped once each in 60% isopropanol and distilled water and washed under running tap water. Sections were mounted with VectaMount aqueous medium (Vector Labs, #H-5501) and imaged within 24 h of staining using a 40× objective on a Nikon Ti2 microscope with a color camera.

Liver H&E histology

A portion of the largest liver lobe was placed in a plastic tissue cassette and fixed for 24 h at 4°C in buffered zinc formalin (Cancer Diagnostics Inc., #171), rinsed with PBS, and stored in PBS at 4°C until processing. Samples were paraffin-embedded (Sakura VIP processor), sectioned at 10 μm on a Leica microtome, and mounted on positively charged glass slides. Sections were stained with hematoxylin and eosin using standard protocols. Multiple nonadjacent sections per liver, spaced 20–40 μm apart in depth to minimize sampling bias, were imaged with a 40× objective on a Nikon Ti2 microscope (color camera) for qualitative assessment of hepatic architecture and lipid-associated vacuolization.

Liver glucocorticoid receptor immunofluorescence

A separate portion of the largest lobe was rapidly frozen in liquid nitrogen–chilled isopentane and stored at −80°C. Three non-serial 10 μm cryosections (50 μm apart) were cut on a Leica CM3050S cryostat and mounted on positively charged glass slides. Sections were thawed at room temperature for 30 min, fixed in 4% paraformaldehyde (Electron Microscopy Sciences, #15710-S) for 10 min, washed 3× in PBS, permeabilized in ice-cold methanol for 10 min, and washed 3× in PBS. After blocking for 30 min (3% BSA, 10% normal goat serum, 0.2% Triton X-100 in PBS), sections were incubated overnight at 4°C in a humidity chamber with primary antibody (anti–glucocorticoid receptor, rabbit monoclonal, clone D6H2L, Cell Signaling Technology, Cat#12041; 1:250) in blocking buffer. Sections were washed 3× for 10 min in PBS/0.2% Tween 20, then incubated for 1 h in the dark with secondary antibody (Alexa Fluor 647 goat anti-rabbit, Invitrogen, A-21245; 1:500) and Hoechst 33342 (Invitrogen, #62249; 1:500) in blocking buffer, and washed 3× for 10 min. Slides were mounted with Fluoromount-G (Electron Microscopy Sciences, #17984-25) and stored at 4°C. Three images per section (nine per liver) were acquired with a 10× objective on a Nikon Ti2 microscope.

Quantitative analysis of glucocorticoid receptor (GR) immunostaining was performed using QuPath software.[38] For each image, a rectangular region of interest (ROI) was defined around the area containing the highest density of sharply focused nuclei. Nuclear segmentation masks were then generated within this ROI via the StarDist plugin utilizing the Hoechst staining channel. These segmentation masks were then used to extract the mean nuclear intensities from the GR staining channel. Final analysis and plotting of single nuclear GR intensity distributions was done using custom scripts on MATLAB (version 2020a).

Measurement of liver triglycerides

Livers were harvested from mice dissected between 2:00 p.m. and 6:00 p.m. The left lateral lobe was immediately snap-frozen in liquid nitrogen and stored at −80°C until analysis. Total lipid extraction was performed using a method adapted from Folch et al.[40] Briefly, ∼100 mg of frozen liver tissue was homogenized in 200 μL saline and 887 μL methanol and sonicated. 1.78 mL of chloroform was then added, samples were vortexed and incubated for 24 h at room temperature. Subsequently, 1.13 mL saline was added, samples were vortexed and centrifuged at 3,748 × g for 15 min at 4°C to induce phase separation.

The lower organic phase containing lipids was collected and allowed to evaporate to dryness in a fume hood for 24 h. Extracted lipids were resuspended in isopropanol, and hepatic triglyceride content was quantified spectrophotometrically using the L-Type Triglyceride M assay (Fujifilm Wako; catalog numbers 994–02891, 990–02991, 992–02892, 998–02992, and 464–01601), according to the manufacturer's instructions.

Briefly, samples and standards were pipetted into a microplate and equilibrated for 5 min at 37°C. Color reagent A was added and incubated for 5 min at 37°C, after which absorbance was measured at 600 nm and 700 nm (first read) to quantify signal arising from free glycerol present in the sample. Reagent B was then added and incubated for 5 min at 37°C, followed by a second absorbance measurement at 600 nm and 700 nm (second read) after enzymatic hydrolysis of triglycerides.

Absorbance at 600 nm measures the quinonimine dye generated by the enzymatic glycerol reaction, whereas absorbance at 700 nm measures non-specific optical background, including light scattering and plate absorbance. For each read, background-corrected absorbance was calculated by subtracting the 700-nm value from the 600-nm value. Triglyceride-specific signal was obtained by subtracting the first background-corrected read from the second background-corrected read. Triglyceride concentrations were determined by comparison to a standard curve.

Measurement of plasma triglycerides and hepatic VLDL secretion rates

Plasma triglycerides and hepatic very-low-density lipoprotein (VLDL) secretion rates were measured to distinguish circulating triglyceride levels during the rest phase, when food intake is minimal, from liver-intrinsic triglyceride export capacity. Circulating triglyceride concentrations reflect the balance between hepatic secretion of triglyceride-rich lipoproteins and peripheral triglyceride clearance, whereas VLDL secretion assays isolate hepatic export independent of clearance.

To measure plasma triglycerides, blood was collected from unfasted mice between 2:00 p.m. and 5:00 p.m. Blood was collected into EDTA-coated tubes, plasma was isolated by centrifugation, and triglyceride concentrations were quantified using the L-Type Triglyceride M assay (Fujifilm Wako), according to the manufacturer's instructions.

Rates of hepatic VLDL secretion were determined following established protocols.[41] Mice were fasted for 5 h starting at 9:00 a.m. and injected retro-orbitally at 2:00 p.m. with the lipoprotein lipase inhibitor tyloxapol (500 mg/kg body weight; Sigma-Aldrich T8761). Tyloxapol inhibits intravascular triglyceride hydrolysis, thereby preventing peripheral clearance of triglyceride-rich lipoproteins and causing plasma triglycerides to accumulate in proportion to hepatic secretion. Because mice were fasted, chylomicron production was negligible, and the accumulating plasma triglycerides predominantly reflect hepatic secretion of VLDL particles.

Tail-snip blood samples (25 μL) were collected into EDTA-containing tubes immediately prior to tyloxapol injection and at regular intervals for up to 4 h thereafter. Plasma triglyceride concentrations were measured using the L-Type Triglyceride M assay, as described above. Hepatic VLDL secretion rates were calculated from the time-dependent linear increase in plasma triglyceride concentration following tyloxapol administration.

Measurement of plasma non-esterified fatty acids (NEFAs)

Plasma NEFA measurements were used to assess insulin-mediated suppression of adipose tissue lipolysis before and during the hyperinsulinemic–euglycemic clamp. Mice were fasted for 5 h prior to blood collection. Blood was collected into EDTA-coated tubes, plasma was isolated by centrifugation and stored at −80°C, and plasma NEFA concentrations were measured using the ACS–ACOD enzymatic method with the NEFA-HR(2) assay (Fujifilm Wako; catalog numbers 999–34691, 995–34791, 991–34891, 993–35191, and 276–76491), according to the manufacturer's instructions.

Percent suppression of plasma NEFA levels was calculated for each mouse as (Basal − Clamp)/Basal × 100, where "Basal" represents plasma NEFA levels measured 10 min prior to initiation of the hyperinsulinemic–euglycemic clamp, and "Clamp" represents plasma NEFA levels measured 145 min after clamp initiation.

Adipose tissue histology and analysis

For subcutaneous white adipose tissue (sWAT), we used the inguinal white adipose depots. For visceral white adipose tissue (vWAT), we used the epididymal white adipose depots. sWAT and vWAT depots were harvested from mice, sliced into small chunks measuring approximately 2 mm × 2 mm, placed into plastic cassettes to allow for good penetration of the fixing solution, and fixed for 24h at 4°C in buffered zinc formalin fixative (Cancer Diagnostics Inc., 171). The tissue chunks were then rinsed with PBS and stored in PBS at 4°C until they were embedded in paraffin in a Sakura VIP instrument. A Leica microtome was used to collect multiple 10 μm-thick sections per sample, which were mounted on positively charged glass slides and stained with hematoxylin and eosin (H&E). Images of H&E−stained sections were captured using a 20× objective on a Nikon Ti2 microscope equipped with a color camera.

Adipocyte cross-sectional areas were quantified in Fiji/ImageJ using the MRI Adipocytes Tools macro toolset (Montpellier Ressources Imagerie; https://github.com/MontpellierRessourcesImagerie/imagej_macros_and_scripts/wiki/Adipocytes-Tools) with the Watershed Algorithm plugin (https://imagej.net/ij/plugins/watershed.html) installed. Each image was first processed with the toolset's background-clearing preprocessing routine using the default parameters (min. size = 40, max. size = 20,000, nr. of dilations = 10, Percentile thresholding). Images from chow-fed groups were then segmented with the simple segmentation routine, and images from HFD-fed groups with the large-magnification segmentation routine, which applies polynomial background flattening before thresholding and performed better on the enlarged adipocytes of these groups. Minimum and maximum particle-size limits were determined empirically for each condition so that the full range of adipocyte sizes present was captured, and were then held constant across all images within that condition. Because adipocyte hypertrophy reduces the number of cells per field, the number of fields analyzed per animal was increased as needed, up to the four available, so that comparable numbers of adipocytes were obtained across groups.

Necropsies

Mice were euthanized and all dissections were performed between 2:00–5:00 PM. All mice were fasted for 5 h prior to necropsy. Tissues were then carefully dissected, excised, and weighed following established protocols.[42] Collected tissues included subcutaneous white adipose tissue (sWAT), visceral white adipose tissue (vWAT), brown adipose tissue (BAT), quadriceps, soleus, gastrocnemius, tibialis anterior (TA), extensor digitorum longus (EDL), liver, spleen, kidneys, heart, pancreas, and small intestine. The small intestine was flushed thoroughly with saline to remove luminal contents prior to weighing, and its total length was measured. All tissues were either processed immediately or snap-frozen for downstream analyses.

Amino acid analysis

Plasma amino acids were extracted as previously described.[43] Briefly, 2 μL plasma was mixed with 100% methanol (−80°C), incubated on dry ice for 5 min, and centrifuged at 16,000 × g for 10 min at 4°C. The supernatant was mixed 1:1 with 80% methanol, centrifuged again, and the final supernatant was collected for LC–MS analysis.

As previously described,[44] plasma amino acids were quantified by liquid chromatography–mass spectrometry (LC–MS) using a QExactive quadrupole-Orbitrap mass spectrometer (Thermo Fisher Scientific) coupled to hydrophilic interaction chromatography (HILIC) via electrospray ionization operating in negative mode. Metabolites were separated on an XBridge BEH Amide column using an acetonitrile–water gradient containing ammonium acetate and ammonium hydroxide. Full-scan data were acquired at 70,000 resolution (m/z 70–1000). The autosampler was maintained at 5°C, and 5–10 μL of plasma extract was injected. Data were analyzed using MAVEN or El-MAVEN software.

Skeletal muscle tissue histology and analysis

Skeletal muscle tissue histology and analysis were carried out using established protocols.[45] Briefly, quadriceps, gastrocnemius, and soleus muscles were excised, with the gastrocnemius and soleus collected as a single specimen for all subsequent histological processing. The entire tissue was placed on a cork disc and surrounded with 10% gum tragacanth (Sigma. Cat. #G1128). This embedded tissue was then frozen in liquid nitrogen-cooled isopentane for 25 s and stored at −80°C until analysis. Frozen muscles were sectioned on a Leica cryostat into 10 μm-thick sections and mounted on positively charged glass slides (Globe Scientific, Cat. # 1354W).

Immunofluorescence staining of fiber types was performed following previously published protocols.[45] Briefly, slides were thawed and air dried at room temperature for 15 min. They were then rehydrated in PBS for 10 min, permeabilized by quickly dipping in 0.3% Triton X-100/PBS, and blocked in 5% goat serum (Jackson ImmunoResearch, Cat. #005–000-121) in PBS for 10 min. Slides were incubated at 4°C overnight with primary antibodies against myofiber type-specific myosin heavy-chain isoforms—MyHC type I (mouse IgG2b monoclonal, DSHB, Cat. #BA-F8, dilution 1:40), MyHC type IIA (mouse IgG1 monoclonal, DSHB, Cat. #SC-71, dilution 1:40), MyHC type IIB (mouse IgM monoclonal, DSHB, Cat. #BF-F3, dilution 1:40)—and against laminin (rat IgG1 monoclonal, Sigma-Aldrich, Cat. #L0663, dilution 1:150) to visualize myofiber boundaries. Slides were washed 3 times for 5 min each in PBS before incubation in secondary antibodies against MyHC antibodies—goat anti-mouse IgG2b (Alexa Fluor 647, Thermo Fisher, Cat. #A21242, dilution 1:800), goat anti-mouse IgG1 (Alexa Fluor 488, Thermo Fisher, Cat. #A21121, dilution 1:800), goat anti-mouse IgM (Alexa Fluor 568, Thermo Fisher, Cat. #A21043, dilution 1:800)—and against anti-laminin antibody (goat anti-rat IgG1, Alexa Fluor Plus 405, Thermo Fisher, Cat. #A48261, dilution 1:500) for 1 h at room temperature on a shaker set to 300 rpm.

Multi-channel fluorescence images were acquired on a Nikon Eclipse Ti2 microscope using a 10× objective. Tiled fields of view were stitched into composite images using NIS-Elements AR software with a 10% overlap. Image analysis was performed in QuPath(v0.6.0).[38] Regions of interest (ROIs) were defined for each image, and myofibers were segmented within ROIs using the laminin channel and the Cellpose 2D deep-learning pretrained model cyto2, implemented via the QuPath Cellpose extension (qupath-extension-cellpose v0.11.0).[39] Myofiber segmentation and feature extraction were performed using a custom Groovy script adapted from an open-source QuPath workflow (Pécot; https://github.com/tpecot/WholeSlideImageAnalysisWithQuPath). For each segmented myofiber, QuPath extracted cross-sectional area (CSA) and mean fluorescence intensity for each myosin heavy-chain (MyHC) channel (type I, IIA, and IIB). Extracted measurements were exported and analyzed in MATLAB, where MyHC fluorescence intensities were used to computationally classify and assign fiber types. CSA distributions were then generated for each fiber type, and histograms were used to compare size distributions across conditions.

Body composition

Fat and lean mass distributions were measured using nuclear magnetic resonance (NMR) coupled with magnetic resonance imaging (MRI) in an EchoMRI 3-in-1 Body Composition Analyzer (EchoMRI LLC, Houston, TX). Individual mice were placed in an EchoMRI animal holding tube, allowed to acclimate to the tube for two minutes and then gently immobilized using the supplied plunger for the duration of the 90 s scan. The fat mass measured by the EchoMRI 3-in-1 Body Composition Analyzer is the mass of all the fat molecules in the body expressed as equivalent weight of canola oil. The lean mass measured is a muscle tissue mass equivalent of all the body parts containing water, excluding fat, bone minerals, and such substances which do not contribute to the NMR signal, such as hair, claws, etc.

Hyperinsulinemic–euglycemic clamp

All hyperinsulinemic–euglycemic clamp experiments were performed during the rest (light) period. All procedures required for the hyperinsulinemic–euglycemic clamp were approved by the Vanderbilt University Animal Care and Use Committee. Five to seven days before the study, catheters were implanted into a jugular vein and a carotid artery of the mice for infusions and sampling, respectively, as described by Berglund et al.[46] Insulin clamps were performed on mice fasted for 5 h using a modification of the method described by Ayala et al.[28] After 3h of fasting, an arterial blood sample was obtained to determine natural isotopic enrichment of plasma glucose. Ninety minutes prior to initiation of the clamp, a quantitative stable isotope delivery to increase glucose isotopic enrichment above natural isotopic labeling was initiated. [6,6-2H2]glucose was primed (16 mg) and continuously infused for a 90 min equilibration and basal sampling periods (0.8 mg/kg/min in saline). The insulin clamp was initiated at t = 0 min with a continuous insulin infusion (2.5–10 mU/kg body weight/min), which continued for 155 min.

Arterial glucose was clamped using a variable infusion rate of glucose + [6,6-2H2]glucose (0.08 MPE), which was adjusted based on the measurement of blood glucose at 10 min intervals during the 155 min clamp period. By mixing the glucose tracer with the unlabeled glucose infused during a clamp, deviations in arterial glucose enrichment are minimized and steady state conditions are achieved. The calculation of glucose kinetics is therefore more robust.[47] Mice received heparinized saline-washed erythrocytes from donors at a rate of 5 μL/min to prevent a fall in hematocrit. Baseline blood or plasma variables were calculated as the mean of values obtained in blood samples collected at −15 and −5 min. Blood was taken from 80 to 120 min for the determination of plasma enrichment. Clamp insulin was determined at t = 100 and 120 min. At 120 min, 13μCi of [^{14}C]2-deoxyglucose ([^{14}C]2DG) was administered as an intravenous bolus. Blood samples were taken between 122 and 155min to determine levels of [^{14}C]2DG. After the last sample, mice were anesthetized, and tissues were freeze-clamped for further analysis.

Plasma insulin was determined by RIA. Plasma glucose enrichments ([6,6-2H2]glucose) were assessed by GC-MS as described previously.[48] Radioactivity of [^{14}C]2DG in plasma samples, and [^{14}C]2DG-6-phosphate in tissue samples were determined by liquid scintillation counting. Glucose appearance (Ra) and disappearance (Rd) rates were determined using steady-state equations.[48] Endogenous glucose appearance (EndoRa) was determined by subtracting the GIR from total Ra. The glucose metabolic index (Rg) was calculated as previously described.[49]

To accurately compare the relative differences in glucose uptake between muscle and fat in both groups, we first had to establish a common baseline due to the significant differences in absolute uptake between tissues. For example, visceral fat in control mice exhibited approximately 10 nmol/min/100g tissue uptake, while gastrocnemius muscle showed approximately 25 nmol/min/100g. Thus, to normalize the data and be able to compare the differences in glucose uptake between tissues, we first calculated the mean uptake for each tissue in the control mice. Thereafter, we divided the glucose uptake measured from each GC-flattened mouse by the mean glucose uptake in the corresponding tissue from control mice.

RNA isolation and quantitative RT-PCR analysis

Gastrocnemius and quadriceps muscles and liver tissue were rapidly harvested, snap-frozen in liquid nitrogen, and stored at −80°C until processing. Total RNA was isolated from frozen tissue using TRIzol reagent (Thermo Fisher Scientific, Cat. #488201) followed by purification with the RNeasy Mini Kit (Qiagen, Cat. #74106) following the manufacturer's instructions. Briefly, 20 mg tissue was first homogenized in 1 mL of TRIzol to lyse the tissue and inactivate RNases. Following the addition of 0.2 mL chloroform for phase separation, the samples were centrifuged for 15 min at 12,000 rpm in 4°C and the aqueous phase containing RNA was collected. 70% ethanol was freshly prepared and then added v/v, and the sample was applied to the RNeasy silica column. Following the manufacturer's instructions, the column was washed to remove residual salts and proteins. An on-column DNase digestion step was also performed to remove residual genomic DNA. Finally, the RNA was eluted in RNase-free water and RNA concentration and purity were assessed by NanoDrop.

Complementary DNA (cDNA) was synthesized from 0.5 to 1 μg of total RNA using the qScript cDNA Synthesis Kit (Quantabio, 95047) according to the manufacturer's protocol. The kit provides a single master mix solution containing an optimized mix of random and oligo(dT) primers, an engineered MMLV RT qScript reverse transcriptase, and a ribonuclease inhibitor protein. 10 μL quantitative PCR reactions were set up using 2.5- to 5-fold dilutions of the synthesized cDNA, gene-specific forward and reverse primers (at a final concentration of 500 nM), and either BlasTaq 2X qPCR MasterMix (ABM, G891) for muscle gene-expression analyses or PowerTrack SYBR Green Master Mix (Applied Biosystems, A46109) for liver analyses. Reactions were run in technical duplicates or triplicates on 384-well plates (Biorad, HSP3905) and a CFX384 Touch Real-Time PCR Detection System (Biorad). Primer sequences are provided in Table S1.

Expression of atrophy and GR target-genes in the quadriceps muscle was normalized to the geometric mean of *Hprt*, *Rplp0*, and *Rpl7l1*. Expression of gluconeogenic and lipid-metabolism–related genes in the liver was normalized to *Hprt*. Relative gene expression was calculated using the ΔΔCt method and expressed relative to the mean of the corresponding control group for each tissue. Because different master mixes were used, gene-expression comparisons were made only within tissue.

Western Blot analysis

Mice were fasted for 5 h. For insulin-stimulated conditions, mice were injected intraperitoneally with insulin at 5 U/kg body weight (Day 21 experiments; Figures 5, 6, and 7A–7G), 0.75 U/kg body weight (Day 60 experiments; Figure S6), or 0.5 U/kg body weight (L-GRKO experiments; Figure 7H). Mice were sacrificed 10 min later, and tissues were collected and snap-frozen. For Western blot analysis, 150 mg adipose tissue, 30 mg liver, or 30 mg skeletal muscle was homogenized in 300–500 μL ice-cold RIPA buffer (Millipore, Cat. #20–188) supplemented with 2× protease and phosphatase inhibitor cocktail (Thermo Scientific, Cat. #1861281). Homogenates were incubated on ice for 30 min and centrifuged at 20,000 × g for 15 min at 4°C. The supernatant was collected and centrifuged repeatedly until the lysate was clear of debris and lipid. Protein concentration was determined using a BCA assay (Thermo Fisher Scientific, Cat. #23227), and lysates were aliquoted and stored at −20°C until immunoblotting.

Protein samples were separated on 4–15%, 4–20%, or 10% SDS-polyacrylamide gels and transferred to 0.45 μm PVDF membranes. Following transfer, membranes were blocked for 30 min in 10% non-fat milk prepared in Tris-buffered saline containing 0.1% Tween 20 (TBST). Membranes were then incubated with primary antibodies diluted in TBST containing 5% BSA for either 2 h at room temperature for GAPDH or overnight at 4°C for other targets. Membranes were washed three times with TBST and incubated with the appropriate secondary antibody for 75 min at room temperature. Depending on the target, membranes were incubated with infrared fluorescent secondary antibodies and imaged using an LI-COR Odyssey imaging system, or with HRP-conjugated secondary antibody and developed using SuperSignal West Pico PLUS chemiluminescent substrate.

The following primary antibodies were used: anti-phospho-AKT Ser473 (Cell Signaling Technology, Cat. #9271), anti-AKT (Cell Signaling Technology, Cat. #9272), anti-GAPDH (Cell Signaling Technology, Cat. #5174), anti-Vinculin (Thermo Fisher Scientific, Cat. #14–9777-80), anti-p85 (Cell Signaling Technology, Cat. #4257), anti-insulin receptor β (Cell Signaling Technology, Cat. #23413), and anti-glucocorticoid receptor (Cell Signaling Technology, Cat. #12041). Secondary antibodies included goat anti-rabbit Alexa Fluor 680 (Thermo Fisher Scientific, Cat. #A21109), IRDye 800CW goat anti-mouse IgG (LI-COR Biosciences, Cat. #926–32210), and HRP-linked anti-rabbit IgG (Cell Signaling Technology, Cat. #7074). All primary antibodies were diluted 1:1,000, and all secondary antibodies were diluted 1:5,000. Blot signals were quantified using LI-COR Image Studio Lite software and further

analyzed in Microsoft Excel. Vinculin served as the loading control for all immunoblots except the Day 60 liver blots shown in Figure S6, for which GAPDH was used. For those blots, values were additionally normalized to a common reference lysate included on each blot to account for inter-blot variability.

QUANTIFICATION AND STATISTICAL ANALYSIS

Unless otherwise indicated, summary data are presented as mean ± SEM. Statistical analyses were performed using GraphPad Prism. Comparisons between two groups were performed using two-tailed unpaired t-tests, with Welch's correction where indicated. Multiple-group comparisons were performed using one-way or two-way ANOVA followed by Tukey's or Šídák's multiple-comparisons tests, as specified in the figure legends. Longitudinal datasets were analyzed using repeated-measures ANOVA, including three-way repeated-measures ANOVA for Time × Diet × Treatment where indicated. VLDL secretion kinetics were analyzed by simple linear regression. Exact statistical tests and sample sizes are provided in the corresponding figure legends. The study was powered ($1-\beta = 0.80$) to detect large effect sizes (>0.67). Results were considered statistically significant at $p < 0.05$. Area-under-the-curve (AUC) for GTT assays, ITT assays, and circadian hormone profiles was calculated using the trapezoidal rule:

$$AUC = \sum_{i=1}^{n-1} \frac{V_{i+1} + V_i}{2} * (T_{i+1} - T_i)$$

where V is the measured value at time T, and n indicates the total number of timepoints.